The anticonvulsant and mood-stabilizing drug valproic acid attracts *C. elegans* and activates chemosensory neurons via a cGMP signaling pathway.

Lucero E. Rogel-Hernandez[1], Helena Casademunt[2], Aravinthan D.T. Samuel[2], Miriam B. Goodman[1]

[1]Department of Molecular and Cellular Physiology, Stanford University, Stanford, CA 94304

[2]Department of Physics and Center for Brain Science, Harvard University, Cambridge, MA 02134

Abstract

Valproic acid (VPA) is a drug with both anticonvulsant and antimanic properties. It has been widely prescribed to treat epilepsy, bipolar disorder, and other neuropsychiatric conditions for decades, but its molecular mode of action in the brain is not fully known. Moreover, prenatal exposure to this drug is linked to developmental anomalies, cognitive deficits, and an increased risk of autism. To determine VPA's effect on the nervous system without requiring systemic drug application and inducing toxic effects, we exploited the well-characterized chemotaxis behavior of the nematode *Caenorhabditis elegans*. We found that *C. elegans* are attracted to VPA, and this behavior is missing in animals lacking the *tax-4* ion channel and the *tax-4*-expressing AWC chemosensory neurons. To test the idea that VPA directly activates the AWC neurons, we performed calcium imaging studies in a line expressing GCaMP6s in all amphid chemosensory neurons in the head. We found that VPA evoked calcium transients consistently in the AWC neurons and variably in AWB and ASH. As cyclic nucleotide-gated channels, the active state of *tax-4* increases upon the binding of cGMP. Within the worm's chemosensory nervous system, receptor guanylate cyclases (rGCs) facilitate the synthesis of cGMP and serve as chemoreceptors for various chemical cues. By performing chemotaxis assays and calcium imaging experiments with rGC mutants against VPA, we found that *odr-1* and *gcy-28* are essential for mediating VPA attraction, as their absence disrupts both behavior and control AWC calcium transients. However, given their broad use in chemosensation, *odr-1* and *gcy-28* most likely act as downstream effectors rather than as direct targets. These findings compelled us to investigate whether chemoreceptors belonging to the G protein-coupled receptor (GPCR) family contribute to VPA sensing. We approached this hypothesis by conducting chemotaxis assays with Gα mutants and identified several (*odr-3*, *egl-30*, *gpa-2;gpa-3*) whose absence leads to a loss of VPA attraction. Thus, future studies should focus on elucidating the mechanisms by which GPCRs contribute to VPA sensing and cGMP signaling.

Introduction

Valproic acid (VPA) is a widely prescribed broad-spectrum antiepileptic drug and a mood stabilizer for bipolar disorder [1]. Although its mode of action in the nervous system remains elusive and unclear, it has been linked to increased GABA levels in the brain [2], an effect proposed to account for VPA's antiepileptic properties [3–6]. Additional candidate signaling mechanisms have been reported, including modulation of arachidonic acid and inositol levels in the brain and indirect inhibition of protein kinase C (PKC) and mitogen-activated protein kinase (MAPK) [Reviewed in [7–9]]. VPA has other effects and molecular targets, including inhibition of histone deacetylase (HDAC), an activity which identifies VPA as a potential cancer therapeutic (clinicaltrials.gov, accessed October 8, 2025) [10,11].

Along with these established and emerging therapeutic benefits, VPA is linked to undesirable effects such as weight gain, hair loss, tremors, pancreatitis, and liver dysfunction [12–15]. Adverse effects arising from prenatal exposure are also significant: in humans and other mammals, studies have shown that prenatal exposure to this drug leads to developmental anomalies in offspring, such as neural tube, limb, and cardiac defects, and increases the risk of autism spectrum disorders [16–21]. Transgenerational effects might not be limited to mothers, since children born to VPA-treated fathers may also have an increased risk of neurodevelopmental conditions [22]. From this brief overview of a large literature, it is evident that improved clarity regarding the molecular targets of VPA in the nervous system might enable the development of safe and efficacious therapeutics to manage the neurological diseases treated with VPA today with an improved risk-reward profile.

The effect of VPA on neural function and behavior has been investigated in several non-mammalian animals and *ex vivo* preparations [23–28], including *Caenorhabditis elegans* nematodes [29–32]. Wild-type *C. elegans* nematodes grown in the presence of VPA display defects in defecation, egg-laying, reduced brood size [29], as well as abnormal DNA methylation [32] and lifespan [30,31]. Whether in mammals or invertebrates, the toxic effects of whole-body exposure to VPA complicate investigations of how this drug affects the nervous system is uncertain. We reasoned that chemotaxis behavior could provide insight into this question without requiring whole-body exposure to the drug,

since *C. elegans* is well-known to navigate chemical gradients and to accumulate near the source of attractants and away from repellants. To achieve this goal, we used *C. elegans* as a chemical detector and adapted our high-throughput chemotaxis-based screening platform [33] to evaluate VPA-induced chemotaxis. *C. elegans* relies on ciliated chemosensory neurons to perform chemotaxis. Each cilium is densely packed with a wide assortment of chemoreceptors that survey the extracellular space for chemical signals [34]. When a ligand activates a chemoreceptor, these proteins translate binding on their surfaces into electrical signals by relaying the information to downstream cyclic nucleotide-gated (CNG) or transient receptor potential (TRP) ion channels via the use of second messengers, such as cyclic nucleotides (cAMP, cGMP) or various lipid-derived mediators (i.e., DAG, IP3), respectively [33,35,36]. CNG or TRP channel activation induces membrane depolarization and initiates behavioral responses to attractant and repellant chemicals in the environment [34].

Chemoreception relies on a variety of receptor types, including receptor guanylate cyclases (rGCs) and G protein-coupled receptors (GPCRs), to enable the detection of environmental cues [37]. Combined, these two classes of proteins account for over 1,700 potential and distinct chemoreceptors in *C. elegans [38,39]*. This immense number and diversity of chemoreceptors renders *C. elegans* one of the most chemically attuned within the animal kingdom [40–42]. Each chemoreceptor can respond to multiple chemicals, and each chemical can activate multiple chemoreceptors, thus granting this organism the ability to discriminate at a minimum between thousands of chemical cues [43]. One can speculate that having a large and diverse repertoire of chemoreceptors could allow for the detection of a more diverse panel of chemicals. Thus, *C. elegans* is a well-suited system to test a variety of ligands, including drugs like VPA. If such ligands are capable of being perceived by *C. elegans,* this creates an opportunity to explore ligand-receptor interactions and to characterize new binding sites, which in turn offers valuable insights into comparative biology that could help identify key human targets to advance biomedical research and drug development [38,39,44].

Combining genetics, high-throughput behavioral studies, and *in vivo* calcium imaging of chemosensory neurons (CSNs), we show that *C. elegans* can detect and respond to the drug, VPA,

through a cyclic nucleotide-dependent signaling cascade. Wild-type animals are attracted to VPA in a manner that depends on the *tax-4* CNG ion channel and the *tax-4*-expressing AWC chemosensory neuron (CSN) pair. Furthermore, attraction to VPA is diminished in mutants for rGC-encoding genes, *odr-1* and *gcy-28*. As cGMP generators, *odr-1* and *gcy-28* may serve as direct VPA targets or act as downstream effectors used by signaling pathways that converge on *tax-4*. This uncertainty led us to explore the possibility that members of the GPCR family, which often signal through Gα subunits, contribute to VPA attraction. Assays with Gα mutants revealed a role for several genes encoding Gα proteins (*odr-3*, *egl-30*, and *gpa-2*;*gpa-3*) in mediating attraction to VPA, and consequently implicating GPCRs in the sensing of this drug. Thus, with its well-defined and highly sensitive nervous system, large repertoire of chemoreceptors, and conserved signaling components, *C. elegans* offers a unique genetic route to the analysis of VPA action.

Methods

Chemical and biological reagents:

We purchased chemicals from the following commercial sources (supplier, catalog no.): valproic acid (APExBIO, B1251), furfural (TCI Chemicals, F00073), isoamyl alcohol (Sigma-Aldrich, W205710), 2-methyl-1-butanol (Sigma-Aldrich, W399817), and valeric acid (Sigma-Aldrich, 240370). We obtained *C. elegans* strains from our in-house collection, the *Caenorhabditis* Genetics Center, other members of the worm community, or derived new strains in-house. Supplementary Table 1 lists the genotypes and origin of all *C. elegans* strains used in this study.

Growth and maintenance of *C. elegans* strains:

We maintained and synchronized animals according to standard methods [45], using N2 (Bristol) worms as wild-type (WT) control. In brief, we grew all strains at 20°C on NGM plates seeded with OP50 *E. coli* as a food source and used well-fed young adult worms for all experiments. We maintained freshly thawed strains for at least three generations before use for behavioral assays [46]. We discarded strains that had

been maintained in the lab for more than 3-4 months and used fresh thaws if needed for additional experiments.

Calcium imaging lines:

In order to measure calcium dynamics in *tax-4(p678), odr-1(n1396), or gcy-28(yum32)* mutants, we introduced transgenes driving expression of GCaMP6s in the nuclei of all CSNs (*aeaIs008[ift-20p::GCaMP6s::3x::NLS]* ?) and mCherry in the cytoplasm (*hpIs728[gpc-1p::mCherry]* X) of a subset of CSNs. Both transgenes were derived from ZM10104, a previously validated, CSN-specific calcium imaging line [47]. Except for our *odr-1* cross, all strains carry the mCherry marker. We verified that lines contained *tax-4(p678)*, *odr-1(n1396)*, and *gcy-28(yum32)* by amplifying genomic DNA with gene-specific primers (see below) and sequencing the PCR-amplified product.

***tax-4* -** Forward: CCAATGGAATTGGCTCTCCTC, Reverse: CATCCCAAGTCAGGATACTG

***odr-1* -** Forward: CGATAATTGGCCTTCTGCTC, Reverse: GGTCAACCTTCGTCCAATCCAC

***gcy-28* -** Forward: agagaaacttttctaaacgtttttcaagaaaagc, Reverse: acttgaagaacggatcgtcctttaatcc

Data acquisition for chemotaxis assays:

We conducted multiple chemotaxis assays in parallel by adapting the workflow previously developed for high-throughput chemotaxis screening of natural products [48]. Briefly, we added 10 mL of chemotaxis media (2.5% Gelrite™ (Research Products International), 5 mM potassium phosphate buffer (pH 6), 1 mM $MgSO_4$, and 1 mM $CaCl_2$) to each well of a 4-well multiwell plate (ThermoFisher, catalog no. 267061). To define the arena within each well, we used foam inserts (MEARCOOH)) with an outer pentagon shape (border of the arena with a top-right notch) and an inner hexagon (the arena itself). Unless otherwise noted, at one of the vertices of the hexagon, close to the notch, we added 2.5 µL of our compound of interest, and to the opposite vertex, 2.5 µL of solvent. Figure 1A illustrates the arrangement, including the craft foam insert design and the placement of the chosen compound and solvent vertices. We

allowed our compounds to diffuse for 60 minutes to establish a chemical gradient in our assays. We washed well-fed young adult worms three times with chemotaxis buffer (5 mM potassium phosphate buffer (pH 6), 1 mM $MgSO_4$, and 1 mM $CaCl_2$) to prevent bacterial interference. To initiate the assays, we added a concentrated drop of worms to the start zone (Figure 1A) using a 200 µL single-channel micropipette and removed excess buffer with PVA eye spears (BVI, catalog no. NC0972725). To monitor the temperature and control relative humidity, we placed our chemotaxis assay plates inside a FORKSPARK® 30L dehumidifying dry cabinet (model: FSDCBLK30). We conducted our experiments at temperatures ranging from 21.9 °C to 25°C, with relative humidity levels ranging from 30% to 39%. We allowed the worms to explore their arena for 60 minutes. To capture the endpoint of the assay, we scanned the assay plates with a consumer-grade flatbed scanner (Epson Perfection V600, model: B11B198011). The focal plane of the scanner was adjusted to match the height of the chemotaxis media, maximizing image contrast [49]. We acquired images (1200 DPI/8-bit grayscale) and saved them as uncompressed *.tiff files. We used the following compounds and concentrations for the experiments in Figure 4C: furfural (20 mM), isoamyl alcohol (9.32 mM), and 2-methyl-1-butanol (20 mM), valeric acid (9.10 M), and valproic acid (6.12 M) [48].

Data curation and analysis for chemotaxis assays:

We assigned a unique identifier to all *.tiff images acquired and the assays represented in each image. We analyzed our images using Our Worm Locator (OWL) Graphical User Interface (GUI) to annotate the worm locations present in each assay [33]. Here, we define a worm location as a region within the arena occupied by at least one worm. For this study, assays with greater than 150 annotated worm locations were included in the analysis [48]. For each strain, we collected data from at least three biological replicates. We aggregated the data for each strain and analyzed it using estimation statistics from the DABEST package (v. 0.3.1) [50]. We generated shared control estimation plots to compare all mutant strains (tests) against wild-type (control). When employing estimation statistics to analyze *C. elegans* responses to VPA, we can infer the following:

1. Positive <Δlocation> (aka bootstrapped mean difference) values whose 95% confidence interval (CI) does not intersect with the zero-intercept indicate that the mutant is, to an extent, more attracted to VPA than the control genotype.
2. For <Δlocation> values whose 95% CI falls at the zero-intercept, indicate that the mutant behavior is indistinguishable from the control genotype.
3. Negative <Δlocation> values whose 95% CI does not intersect with the zero-intercept correspond to the mutant having a partial or a complete loss of attraction to VPA compared to the control genotype.

In addition, we applied this statistical approach to compare the mean worm locations of animal populations exposed to different concentrations of VPA (tests) versus those exposed to water (control) (Figure 1B). Furthermore, to provide insights into how the <Δlocation> functions under different VPA concentrations, we decided to fit our data from Figure 1B to the Hill equation (Figure 1C), which is primarily used to describe dose-response relationships [51,52]. Here, the Hill equation is represented in the following manner:

$$y = E_{max} \times ([C]^n / EC50^n + [C]^n)$$

Where y represents the <Δlocation> at a concentration of VPA ([C]), E_{max} is the maximum <Δlocation>, and *EC50* is the VPA concentration at which the <Δlocation> is half of the maximum. *n* is the Hill coefficient, which determines the steepness of the curve and was set to 1 to indicate a non-cooperative relationship [51]. Supplementary Table 2 lists the mean worm location values for strains tested against VPA and other chemicals (refer to Figure 4C). Supplementary Table 3 lists the <Δlocation> values and their 95% CI quantified with the DABEST package for comparisons between control and test groups.

Data acquisition for calcium imaging:

We performed calcium imaging experiments, as previously described by Lin et al. (2023) [47]. To capture the calcium dynamics of the 11 amphid CSN pairs, we immobilized individual transgenic *C. elegans* expressing the calcium indicator GCaMP6s in the nuclei of these neurons in a microfluidic device. To

enable post-hoc neuronal identification, these animals also expressed cytoplasmic mCherry in the AFD, ASE, ASI, ASJ, AWB, and AWC neurons [47]. Transgenic animals retained the ability to migrate towards VPA in behavioral assays, underscoring their utility for determining cellular responses to VPA. Unexpectedly, these transgenic animals are more strongly attracted to VPA than wild-type: <Δlocation> = 4.15 ± 95% CI [3.39, 4.88] mm. We exposed their noses to controlled pulses of VPA diluted with imaging buffer (mM): potassium phosphate (5, pH 6), $MgSO_4$ (1), $CaCl_2$ (1), and NaCl (50), adjusted to 350 mOsm with sorbitol (VPA final concentration: 6.12 x 10^{-4} M). Each animal underwent six 10-second pulses of VPA, separated by 30-second intervals of VPA-free imaging buffer. We repeated this procedure 2-4 times per animal to assess which amphid CSNs responded to VPA. To monitor the neuronal responses of *C. elegans* to VPA, we used a spinning-disk confocal microscope equipped with a 60X objective, capturing volumetric data at 2.5 (control, *tax-4*, *odr-1*) frames per second (fps), 1.6 fps (*gcy-28*), or 1.2 fps (*tax-4*) [47]. We recorded 62% of *tax-4* animals at 2.5 fps and 38% at 1.2 fps. We used a 488-nm laser to excite GCaMP6s and a 561-nm laser to excite mCherry.

Data curation and analysis for calcium imaging:

We assigned unique identifiers to each animal and its corresponding recordings to manage and process the raw data. We obtained recordings across four strains: control (ZM10104), *tax-4* (GN1103), *odr-1* (GN1126), and *gcy-28* (GN1136). The number of animals recorded from each strain is as follows: control (N = 21 animals), *tax-4* (N = 21), *odr-1* (N = 7), and *gcy-28* (N = 5). From these animals, we collected a total of 155 recordings: control (N = 59 recordings), *tax-4* (N = 61), *odr-1* (N = 21), and *gcy-28* (N = 14). Because the frame rate we used to acquire image stacks varied between 1.2 and 2.5 fps (see above), we interpolated all datasets to 2.5 fps (control, *tax-4*, *odr-1*) or to 1.6 fps (*gcy-28*) prior to analysis. We used MATLAB to perform all image processing tasks, which included identifying and tracking CSNs, extracting their corresponding calcium signals, normalizing these signals, and averaging them per CSN pair across animals [47]. Refer to Lin et al. (2023) for details regarding identifying, tracking, and analyzing individual neurons [47]. Briefly, for each recording, the orientation of each animal was determined to properly locate the positions of all anterior CSNs. Given that ASH and ASJ are easily

distinguishable from the rest, we annotated these two neuronal pairs first, followed by three pairs that are close to each other: ASK, ADL, and ASI [47]. We annotated the rest of the cells with the guidance of the cytoplasmic mCherry marker and with respect to their position to the easily identifiable neurons [47]. An experienced observer assigned each neuron its identity based on the well-defined neuroanatomy of the *C. elegans* nervous system [53] and the position of each neuron relative to the body, feeding organ (pharynx), and to mCherry-expressing neurons. We would like to note however, that the level of confidence in annotating CSNs in the *odr-1* mutant background was reduced due to the absence of the mCherry marker and reduced responses to VPA stimulation. Other instances in which it was difficult to annotate the identity of CSNs occurred when the neurons were too close to each other or didn't display any activity. To track the CSNs over time, we made use of a neighborhood correlation tracking algorithm, where the center of each neuron and its surrounding 3D neighborhood are tracked independently from frame to frame [47]. The baseline fluorescence was determined individually for each recorded neuron. Fluorescence F_0 was monitored over time and corrected for photobleaching; we reported signals as $\Delta F/F_0$ [47]. We proofread the resulting traces and excluded any that (a) showed signal mixing with neighboring neurons (we confirmed this by verifying neuron overlap in the recorded images); (b) showed signs of mistracks (e.g. sudden signs in activity caused by the tracked point jumping to a different nearby neuron); or (c) showed large changes in baseline activity during the recording (sometimes caused by motion artifacts when the head of the worm drifts over time) that prevented us from establishing a consistent F_0.

To compare the different calcium imaging lines to the control during VPA presentation and assess the drug's effect, we computed the mean global signed max $\Delta F/F_0$ value (Supplementary Table 4) for each CSN pair for each calcium imaging line and scored statistical significance by using the Mann-Whitney U test (Supplementary Table 5) [54]. As a first step, we applied a Savitzky-Golay filter with third order polynomial to each recording to smooth the signals and reduce noise. We then proceeded to assess the magnitude of the response for each CSN pair to VPA by identifying both their global maximum and minimum values within the time window in which the drug was applied, and the one with the larger

absolute value was selected as the signed max $\Delta F/F_0$ value. We employed this single-point metric to accommodate the natural variability in responses across all eleven pairs of CSNs to VPA.

Data and Code Availability:

The code for OWL can be accessed on GitHub: https://github.com/Neuroplant-Resources/Neuroplant-OWL.git via a digital object identifier, DOI: https://doi.org/10.5281/zenodo.7807007.

Results

C. elegans is attracted to VPA in a dose- and *tax-4*-dependent manner.

Although it is well-established that VPA has valuable therapeutic benefits for the treatment of epilepsy and bipolar disorder, the chemical signaling pathways engaged by VPA in the nervous system remain enigmatic. To address this knowledge gap, we took an unconventional approach and explored the possibility that VPA induces chemoattraction or repulsion in *C. elegans*. Using a high-throughput chemotaxis-based platform [33], we found that wild-type (WT) animals are attracted to VPA and that the strength of attraction increases with the source concentration (Figure 1B). The EC_{50} for attraction is 0.39 M at the source location. To evoke the strongest possible behavioral response, we delivered this drug in its pure form (6.12 M) at the source position for all subsequent behavioral phenotyping tests. Notably, animals are not immersed in VPA during these assays, minimizing the risk of toxic effects. Our finding that animals are able to migrate toward the VPA source implies that they can sense VPA at the starting zone, where the concentration is likely to be several orders of magnitude less than that at the source.

Next, we sought to evaluate the role of the chemosensory nervous system in mediating this behavior. Eleven pairs of ciliated CSNs reside in the amphid sensilla in the head and five in the phasmid sensilla in the tail [34]. Although these CSNs possess distinct sensory functions, they share a similar shape [34,55]. Thus, to assess if one or multiple CSN pairs detect VPA, we tested *dyf-7* and *oig-8* mutants

with defects in sensory dendrites or cilia. Without functional *dyf-7*, a subset of head CSNs fail to extend their dendrites to the tip of the nose, while the cilia and axons develop normally [56]. This morphological defect displaces the cilia and its chemoreceptors further away from the nose opening, thereby reducing their exposure to several environmental chemical cues and ultimately impairing their ability to detect them [55,57]. Meanwhile, *oig-8* mutants give rise to animals with decreased ciliary branching in AWA, AWB, and AWC CSNs [58].

In surveying the ability of *dyf-7* and *oig-8* mutants to sense VPA via the use of chemotaxis assays, we found that both mutants exhibit a reduction in attraction to this drug in comparison to wild-type animals, as indicated by a negative <Δlocation> value. This finding implicates ciliated sensory neurons in VPA attraction and given the effects of both mutants on CSN structure, the behavioral deficit is likely to reflect disruption in the first steps of VPA sensing. Next, we tested mutants defective in the *tax-4* (CNG) and *osm-9* (TRP) ion channels required for chemosensory transduction [34]. We found that *tax-4;osm-9* double mutants are indifferent to VPA (Figure 1E), confirming the central role for CSNs and chemosensory signaling in VPA sensing. Since these ion channels are differentially expressed within the chemosensory nervous system, we tested single mutants for these two channels to narrow VPA's site of action [33]. We found that only *osm-9* single mutants, but not *tax-4* mutants, were attracted to the drug (Figure 1E). Unexpectedly, VPA attraction was modestly enhanced in *osm-9* single mutants (Figure 1E), suggesting that, similar to attraction to isoamyl alcohol and 2-methyl-1butanol [59], *osm-9* functions as a negative regulator of VPA attraction. Together, these findings strongly implicate sensory cilia and one or more *tax-4*-expressing CSN as the primary receptor neuron for VPA, enabling attraction to this drug.

VPA attraction relies on the *tax-4*-expressing AWC chemosensory neuron pair.

Having established that *C. elegans* is attracted to VPA in a *tax-4*-dependent manner, we next sought to determine which *tax-4*-expressing neurons are required for this behavior. To achieve this, we collected mutants overexpressing constitutively active caspases under cell-specific promoters, a strategy that induces apoptosis and eliminates the target cell [60]. For nine out of the ten *tax-4*-expressing CSNs

(Figure 2A), we tested the ability of mutants lacking individual CSN pairs (AWB, AWC, ASG, ASI, ASJ, and ASK) or in combination (AQR, PQR, and URX) to detect VPA [61,62]. To assess whether ASE plays a role in VPA sensing, we tested mutants lacking the *che-1* transcription factor, which is required for ASE identity and function [63]. In addition to assessing the roles of these *tax-4*-expressing CSNs in detecting VPA, we also tested animals lacking two *osm-9*-expressing CSNs, ASH and AWA, with the expectation that they might behave similarly to *osm-9* mutants. For ASH, we used a line expressing constitutively active caspases under an ASH-specific promoter [64]. For AWA, we assessed the ability of *odr-7* mutants to respond to VPA, as this mutant fails to detect AWA-sensed chemicals and is reported to adopt an AWC-like fate [65,66].

In comparing the behavior of these mutants to those of intact, wild-type animals, it is clear that animals lacking the *tax-4* expressing CSN pair AWC contribute significantly to the detection of VPA (<Δlocation> = -6.76 ± 95% CI [-7.37, -6.16] mm) and respond similar to mutants lacking *tax-4* (<Δlocation> = -10.05 ± 95% CI [-10.78, -9.36] mm) (Figure 2B). The remaining *tax-4* expressing CSNs contribute moderately (AQR, PQR, URX, abbreviation: A/P/U-), minimally (ASJ, ASG), or not at all (ASK, AWB, ASE, and ASI) to VPA attraction (Figure 2B). As proposed above, animals missing the *osm-9*-expressing ASH CSN pair are slightly more attracted to VPA (<Δlocation> = 2.33 ± 95% CI [1.58, 3.14] mm) than wild-type and display similar responses as those observed for *osm-9* single mutants (Figure 1E, <Δlocation> = 3.44 ± 95% CI [2.75, 4.13] mm). On the other hand, *odr-7* mutants with disrupted AWA neuron fate behave like wild-type and remain attracted to VPA. These findings demonstrate that AWC neurons are absolutely required for VPA attraction and leave open the possibility that additional CSNs may contribute to this behavior.

To determine whether or not *tax-4* is required in the AWC neurons, we restored wild-type *tax-4* expression to the AWC in a *tax-4* null background (Figure 2C). We found that wild-type *tax-4* expression in AWC alone was sufficient to re-establish wild-type VPA attraction, indicating that *tax-4* acts cell-autonomously within the AWC neurons to promote VPA attraction. By contrast, restoring wild-type *tax-4* to ASI, which provides synaptic input to AWC [53], had no effect on VPA attraction (Figure 2C).

Unlike most other CSN pairs, the AWC pair exhibits asymmetric expression of chemoreceptors [67]. The AWC^{ON} neuron expresses the GPCR *str-2*, while the AWC^{OFF} neuron lacks *str-2* expression and expresses the GPCR *srsx-3* [68]. Each worm contains one AWC^{ON} and one AWC^{OFF} neuron [67]. To investigate whether one or both AWCs mediate attraction to VPA, we conducted chemotaxis assays with mutants that give rise to either two AWC^{ON} (*nsy-1*) or two AWC^{OFF} (*nsy-4*) neurons [68]. Like animals lacking AWC neurons entirely, *nsy-1* mutants lacking AWC^{ON} neurons and *nsy-4* mutants lacking AWC^{OFF} neurons are not attracted to VPA (Figure 2D), suggesting either that both types of AWC neuron contribute to VPA-evoked chemotaxis or that some factor conferred by asymmetry in AWC signaling is needed for this behavior. These findings reinforce two ideas, namely that *tax-4* acts within the AWC neurons and this pair of CSNs are essential for VPA attraction.

VPA evokes *tax-4*-dependent calcium transients in AWC, AWB, and ASH.

To better understand the contribution of the AWC and other CSNs in VPA-sensing in an intact animal, we imaged VPA-evoked changes in intracellular calcium in all amphid CSNs [47], superfusing the animal's nose with VPA diluted to a final concentration of 0.6 mM in physiological saline, mirroring the range (0.35-0.69 mM) found in the plasma of VPA-treated patients [69–72]. In control animals, the AWC and AWB CSNs stood out as VPA-sensitive (Figure 3, Supplemental Figure 1A). These experiments revealed that the AWC neurons act as the primary cellular sensors for VPA, agreeing with our results from the chemotaxis assays with lines missing different CSN pairs. The AWC neurons responded consistently and robustly to VPA, evoking large negative calcium transients upon its presentation and large positive calcium transients upon its removal (Figure 3). These so-called OFF responses are a hallmark of AWC chemosensory transduction and are consistent with prior studies of AWC responses to other chemical stimuli [47,73–77]. Interestingly, the AWB neurons responded to VPA presentation in an ON manner in roughly one out of every four animals (Supplementary Figure 1A). The variability observed in AWB could stem from differences in gene expression among animals or that the AWB neurons are less sensitive to VPA and would exhibit stronger responses to higher VPA doses. These findings underscore the central

role of the AWC neuron pair in VPA sensing and establish that, similar to neurons in other animals, including mammals [23–28,70,78–90], *C. elegans* neurons are sensitive to submillimolar concentrations of VPA.

To determine how the *tax-4* CNG channel contributes to VPA sensing by CSNs, we recorded the activity of all amphid CSNs in a *tax-4* null background (Figure 3, Supplemental Figure 1B). Consistent with a central role for *tax-4* in VPA-evoked signaling, loss of *tax-4* abolished VPA-evoked calcium transients in AWC and AWB. Additionally, we observed modest *tax-4*-dependent VPA-evoked responses in ADF, ASE, ASH, ASJ, and ASK (Figure 3, Supplementary Figure 1), suggesting that these neurons might also contribute to VPA sensing to a minor extent. Unexpectedly, loss of *tax-4* increased the frequency (50% vs. 42% of trials in *tax-4* and control animals) and amplitude of VPA-evoked calcium transients in the ASH neurons (Figure 3, Supplementary Figure 1). Because the ASH neurons do not express *tax-4*, these findings imply that the contribution of ASH to VPA sensing depends on modulation by a *tax-4*-expressing CSN. Thus, VPA-evoked calcium transients are *tax-4*-dependent in 7 of 11 amphid CSN pairs studied via calcium imaging and this finding links VPA to cyclic nucleotide-dependent signaling in multiple *C. elegans* sensory neurons.

Given that the ASE and AWC neurons respond to VPA and both pairs exhibit left-right asymmetry [91], we analyzed VPA-evoked calcium transients in the left and right neurons before averaging them together (Supplemental Figure 2). From this analysis, we found that the calcium transients observed for the ASE CSN pair are driven primarily by ASER activation, with the majority of the responses showing a decrease in calcium activity when exposed to VPA (Supplemental Figure 2). These responses were absent in the *tax-4* mutant background (Supplemental Figure 2). In contrast to the ASE pair, both AWCs responded consistently to VPA (Supplemental Figure 2), which is consistent with our behavioral studies demonstrating a role for both AWC^{ON} and AWC^{OFF} in VPA sensing (Figure 2D). However, since the identity of the AWC CSNs is stochastic, we are not able to link responses to the left and right AWC neurons to their identities as AWC^{ON} or AWC^{OFF} identities [92]. The calcium transients in both AWCL and AWCR observed in WT are missing in the *tax-4* mutant background (Supplemental

Figure 2), demonstrating that both cells facilitate VPA attraction through *tax-4*-dependent signaling pathways. In summary, *in vivo* calcium imaging affirms the central role of the AWC neurons in VPA sensing and implicates AWB and ASH as additional signaling partners.

Two receptor guanylyl cyclase genes, *odr-1* and *gcy-28*, are required for VPA attraction.

Given the dominant role of AWC in both cellular and behavioral responses to VPA and its dependence on expression of the *tax-4* CNG ion channel gene, we next sought to identify the receptor guanylyl cyclases (rGCs) involved in VPA attraction. This class of membrane proteins enables *tax-4* activity via cGMP synthesis [34]). If an rGC is indeed involved in the process, these experiments would also argue against the possibility of VPA directly modulating TAX-4-dependent ion channels. We initiated our exploration by analyzing the VPA-evoked behavior of mutants lacking five rGC genes known to be expressed in AWC (Figure 4A; Refs. [93–95]). In doing so, we found that the behavior of *gcy-14, gcy-12,* and *gcy-20* performed similarly to wild-type or exhibited minor defects (Figure 4B), indicating that these three rGCs are unlikely to be involved in VPA sensing. Conversely, loss of *odr-1* and *gcy-28* function rendered animals indifferent to the drug (Figure 4B).

Because *odr-1* and *gcy-28* have been previously implicated in sensing other chemical stimuli [34,75,96], it seems unlikely that either rGC confers chemical specificity. We directly tested this inference by assaying *odr-1* and *gcy-28* mutants for their ability to detect four additional compounds: furfural (FUR), isoamyl alcohol (IAA), 2-methyl-1-butanol (2M1B), and valeric acid (VA), an analog of VPA [48,97]. We selected this panel of compounds because we, as well as others, have shown that at specific concentrations, these compounds are attractive to *C. elegans* in a *tax-4*-dependent manner [48,59,75]. In doing pairwise comparisons between each mutant and wild-type animals for every compound tested, we found that we can recapitulate previous findings; attraction to all these compounds relies on *tax-4* signaling pathways, and *odr-1* is required for IAA attraction (Figure 4C) [96]. In addition to mediating attraction behaviors to VPA and IAA, *odr-1* is essential for mediating similar behaviors to FUR, 2M1B, and VA (Figure 4C). On the other hand, *gcy-28* is crucial for mediating attraction to VPA and 2M1B, as

its absence leads to a reduction in sensitivity to these compounds (Figure 4C). Interestingly, *gcy-28* mutant animals appear slightly more attracted to FUR, IAA, and VA relative to wild-type and these responses were indistinguishable from one another (Figure 4C). Thus, *odr-1* in is required to detect our entire panel of attractants and *gcy-28* is required for attraction to 2MIB and VPA. From these findings, we infer that neither rGC is a candidate VPA receptor, but that one or both function as downstream effectors of VPA receptors.

To assess whether *odr-1* and *gcy-28* are essential for facilitating VPA sensing in AWC, we monitored the calcium transients of this CSN pair in response to VPA in mutant backgrounds (Figure 4D). These experiments revealed that in the absence of either rGC, the calcium transients observed in control animals for AWC during VPA presentation are absent, similar to the *tax-4* mutant background (Figure 4E). This was also the case for AWCL and AWCR (Supplementary Figure 3), suggesting that *odr-1* and *gcy-28* are tightly linked to VPA sensing in both AWC^{ON} and AWC^{OFF}. Given that ODR-1 is primarily concentrated in the cilia, while GCY-28 is confined to the axons, it is tempting to postulate that they work together in a two-step signaling pathway to relay VPA detection and activate the AWC neurons with cGMP acting as the key secondary messenger in both locations [98].

Aside from AWC, we also captured the calcium transients of the remaining amphid CSN pairs to VPA in *odr-1* and *gcy-28* mutant backgrounds (Supplementary Figure 4). Similar to AWC, the calcium transients previously observed in AWB are absent in *odr-1* and *gcy-28* (Figure 4D, 4E). However, given AWB's variability in VPA-evoked calcium transients, we cannot exclude the possibility that these mutants do not affect VPA-evoked calcium transients in AWB (Figure 4E). Interestingly, the ASH neurons, much like in control and *tax-4* backgrounds, still respond to VPA, and in a more pronounced manner in the *odr-1* background (Figure 4D, 4E).

Additionally, we found that the small and variable *tax-4*-dependent calcium transients observed for ADF are mediated by *gcy-28,* while those for ASK, ASJ, and ASE are not mediated by either rGC (Supplementary Figure 5). Given that ASE is an asymmetric pair, and in control animals, most responses to VPA are mediated by ASER, we analyzed calcium transients of the left and right ASE neurons

independently from one another to assess if averaging these pairs together obscured valuable insights (Supplementary Figure 3). Similar to control animals, ASER responded to VPA in a subset of recordings in both mutant backgrounds and thus, neither rGC is essential for facilitating this cell's ability to detect VPA (Supplementary Figure 3). Since ASER activity relies on *tax-4*, it is very likely that another rGC is involved in the detection process that may or may not be a direct target for VPA.

In short, we identified an important role for *odr-1* and *gcy-28* in VPA-evoked calcium transients in the AWC, AWB, and ASH neurons, but not in the ASE neurons. These results inform a model where attraction to VPA engages multiple CSNs to induce a certain level of attraction and this behavior is strongly driven by cGMP-dependent signals with overlapping, but non-identical molecular signaling pathways. The central role of the AWC neurons in VPA attraction further supports a model in which these neurons detect VPA in a manner that depends on the ODR-1 and GCY-28 rGCs and the TAX-4 ion channel proteins and that none of these three proteins confer selective sensitivity to VPA or bind VPA.

Disruption of G protein signaling impairs VPA attraction.

What other class of chemoreceptor proteins might grant the AWC neurons the ability to detect the presence of VPA? G-protein coupled receptors (GPCRs) are cell surface receptors that facilitate physiological responses to various chemical stimuli, including odorants and tastants [99]. Similar to the model emerging from this study for VPA-evoked signaling in AWC, signaling pathways that mediate vertebrate vision and olfaction depend on GPCRs that converge on CNG channels and include G proteins and rGCs as intermediate effectors [100]. Whereas the *C. elegans* genome contains ~1,675 genes predicted to encode GPCRs [39], there are only 21 genes encoding Gα subunits [101], 1 encoding β-arrestin [102], and 13 genes encoding regulators of G protein signaling (RGS) [103]. As illustrated in Figure 5A, all of these genes encode for proteins that are central to classical GPCR signaling [104,105]. First, we obtained mutants defective in the function of 8 (of 10) genes encoding Gα proteins expressed in the AWC neurons (Figure 5B) and tested them for their ability to display VPA attraction. In this way, we identified at least four Gα genes required for VPA attraction (Figure 5C). The *odr-3*, *egl-30*, and the

double mutant *gpa-2;gpa-3* displayed the most severe defects in VPA attraction (Figure 5C). Since our *gpa-2;gpa-3* double mutant exhibited a strong defect, we compared the behavior of *gpa-2* and *gpa-3* single mutants to WT. Interestingly, *gpa-2* mutants show a slight increase in attraction to VPA compared to WT, whereas *gpa-3* mutants exhibit a decrease in attraction to VPA. These results indicate that *gpa-2* and gpa-*3* have distinct roles in the neural circuit pathway responsible for mediating VPA attraction, and the absence of both disrupts the pathway's function more severely than either mutation alone. The *odr-3* mutant was significantly impaired in detecting VPA (Figure 5C). Notably, *odr-3* expression is limited to the chemosensory nervous system. Although *odr-3* mutations are known to disrupt the morphology of AWC cilia [106], such morphological defects do not necessarily impair AWC signaling [107]. Thus, *odr-3* is a strong candidate Gα gene for mediating VPA sensing. The other Gα mutant with a large effect, *egl-30*, also implicates a GPCR in mediating attraction to VPA (Figure 5C). However, because *egl-30* mutants exhibit a sluggish phenotype, we cannot determine whether the observed behavioral defect is due to a loss of VPA sensing or changes in movement. The remaining Gα mutants tested were more similar to wild-type (Figure 5C), suggesting that they have little or no influence on the overall response to VPA. Although further research is needed to determine which of the four candidate Gα subunits is required for VPA attraction and contribute to VPA-sensing by the AWC neurons, these results establish a role for G proteins and potentially GPCRs in VPA sensing.

To further evaluate the role of GPCR signaling in AWC, we conducted chemotaxis assays with *rgs-2* and *rgs-3* mutants (Figure 5D). These genes encode RGS proteins, which function to enhance the activity of Gα proteins, promoting their transition to the inactive GDP-bound state (Figure 5A) [103]. The gene *rgs-2* is expressed broadly within the worm, including in the AWC neurons [108]. On the other hand, *rgs-3* is exclusively expressed in nine pairs of CSNs, including the AWC neurons [109]. Without *rgs-2* or *rgs-3*, the animals no longer respond to VPA to the same extent as wild-type (Figure 5D). Unexpectedly, loss of RGS function decreases sensory response because, as negative regulators of G protein signaling, their absence should lead to prolonged signaling. However, previous reports indicate that loss of *rgs-3* increases GPCR signaling while reducing sensory responses by decreasing synaptic transmission

[34,109]. From these reports, we can speculate that this is likely what is happening in *rgs-3* mutant AWC neurons, which leads to indifference to VPA.

Additionally, we surveyed the ability of *arr-1*, *grk-1*, and *grk-2* to detect VPA (Figure 5E). The gene *arr-1* encodes for arrestin, while *grk-1* and *grk-2* encode for two distinct GPCR kinases (GRKs). Among other functions, GRKs and arrestin work together to desensitize GPCRs, thereby protecting cells from receptor overstimulation (Figure 5A) [110–112]. Signaling through many GPCRs via G proteins typically ends with the phosphorylation of the active receptor by GRKs, followed by arrestin binding and receptor internalization [111]. Our chemotaxis assays revealed that *arr-1* and *grk-1* mutants behave like wild-type, whereas *grk-2* mutants were defective in VPA attraction. Previous studies with other chemicals have observed similar behavioral patterns between wild-type and these mutants and cannot link them directly to chemosensation [34,102]. However, the *arr-1* mutant has been linked to chemosensory adaptation [102]. Thus, we cannot conclude that these mutants are attracted to VPA due to receptor overstimulation. Unlike *grk-1* and *arr-1*, previous research has demonstrated a role for *grk-2* in chemosensation [113–115]. Collectively, these findings show that VPA attraction requires at least one Gα protein, one RGS, and one GRK and is likely to be independent of arrestin, supporting a role for at least one GPCR serving as a molecular target for this drug.

Discussion

Using *C. elegans* chemotaxis behavior as a screening tool, we showed that this simple animal is attracted to the anticonvulsant and mood-stabilizing drug, VPA. This whole-animal behavioral phenotype relies on chemosensation since smell- and taste-blind *tax-4;osm-9* double mutants are insensitive to VPA. In this study, we further show that VPA attraction requires an intact pair of AWC chemosensory neurons and that their contribution to behavior requires an intact *tax-4* CNG-gated ion channel gene. The *tax-4* functions cell-autonomously within the AWC neurons, suggesting that AWC relies on a cyclic nucleotide-based signaling cascade to detect and respond to VPA. With *in vivo* chemosensory neuron-specific calcium imaging, we demonstrate that AWC activity is suppressed in the presence of VPA and exhibits a robust

OFF response, reminiscent of the modulation cytoplasmic calcium in AWC neurons stimulated by a number of other odorant ligands [47,73–77]. All aspects of this VPA-evoked response are eliminated by loss-of-function mutations in *tax-4* and in two rGC-encoding genes, *odr-1* and *gcy-28*. Collectively, these findings imply that VPA sensing depends on the activation of the AWC neurons and that VPA activates a signaling cascade that uses cyclic nucleotides as a cytoplasmic second messenger. Our genetic dissection studies implicate additional signaling partners in VPA attraction, including four genes encoding G protein α subunits, *odr-3*, *egl-30*, *gpa-2*, and *gpa-3*, two genes encoding regulators of G protein signaling (RGS) proteins, *rgs-2* and *rgs-3*, and one gene encoding a GPCR kinase (GRK), *grk-2*. All of these G-protein related genes are expressed in the AWC neurons [95,101,116], marking them as candidate signaling partners accounting for VPA sensing by the AWC neurons. Although additional work will be needed to clarify their precise contribution to VPA sensing, the picture emerging from these findings is that VPA engages a CNG-mediated signaling cascade in the AWC neurons.

Multiple chemosensory neurons detect VPA and contribute to attraction

The AWC neurons are not the only CSNs that contribute to VPA attraction or that generate CNG-sensitive calcium transients upon exposure to VPA, however. Loss of the ASH neurons increases VPA attraction (Fig. 2B), which was unexpected given the tight association between ASH signaling and aversive responses [34]. Although the *odr-1* gene is not known to be expressed in the ASH neurons, loss of *odr-1* rGC function increased VPA- evoked calcium transients in the ASH neurons (Fig. 5). This effect might arise through conventional synaptic signaling or by negative regulation of ASH function mediated by cGMP transferred from *odr-1*-expressing neurons via gap junctions, as previously proposed for other ASH-dependent behaviors [117]. Three other pairs of chemosensory neurons showed *tax-4*-sensitive calcium responses: AWB, ADF, and ASK (Figure 3, Supplemental Figure 5). Similar to the AWC neurons, VPA-evoked calcium responses in AWB were absent in *tax-4*, *odr-1*, and *gcy-28* mutant animals (Figures 3, 5). Distinct from the AWC neurons, which showed robust VPA responses in every control animal, the AWB neurons responded to VPA in a subset of animals. This variability might indicate that

AWB is less sensitive to VPA than AWC, despite sharing a similar dependence upon *tax-4*, *odr-1*, and *gcy-28*. The engagement of multiple CSNs in VPA attraction and the unique genetic footprint of VPA-evoked calcium transients exhibited by each of the VPA-sensitive neurons (AWC, AWB, ASH) may indicate that each of these CSNs has a distinct VPA chemoreceptor(s), or that the sensitivity of the CNG signaling cascade differs among them, or a combination of these factors.

The receptor guanylate cyclases required for VPA attraction contribute to sensing other chemicals

In addition to their role as enzymes that catalyze the synthesis of cGMP from GTP, rGCs also function as receptors for peptides and other chemical cues [118–120]. Prior studies in *C. elegans* implicate *odr-1* in chemotaxis responses to isoamyl alcohol, butanone, benzaldehyde, indole, and 2-heptanone [96,121,122] and *gcy-28* in butanone responses [98]. Consistent with the idea that these rGCs play a ligand-independent role in VPA chemotaxis, we found that *odr-1* is required for attraction not only to VPA, but also to isoamyl alcohol, furfural, 2-methyl-1-butanol, and valeric acid and that *gcy-28* is needed for attraction to VPA and 2-methyl-1-butanol. In addition to its expression in AWC, *odr-1* is expressed in ASI, ASJ, ASK, and AWB [93]. None of these CSN pairs responded to VPA as robustly as AWC in our calcium imaging experiments. Similarly, *gcy-28* transcripts are detected in most CSN pairs [94,95], but only a subset of CSNs are sensitive to VPA. Thus, neither *odr-1* nor *gcy-28* expression is insufficient by itself to confer sensitivity to VPA and both are required for attraction to multiple chemicals. Collectively, these findings imply that the contribution of *odr-1* and *gcy-28* to VPA sensing resides primarily in their enzymatic activity.

VPA converges on a cGMP-gated ion channel and relies on cGMP synthesis

The AWC chemosensory neurons respond to chemical stimuli in a manner that is analogous to OFF responses in vertebrate photoreceptors [123], including the modulation of a cGMP-gated ion channel. The AWC neurons respond similarly to VPA (Fig. 2) as they do to other compounds and complex mixtures [47,74–77,123]. Here we show that ligand-induced decreases in intracellular Ca^{2+} and

OFF responses in AWC require the *tax-4* CNG ion channel gene and the *odr-1* and *gcy-28* rGCs. These findings support a model in which TAX-4 ion channels are open in the absence of chemical stimuli and closed during chemical stimulation [124] and that these changes in ion channel activity mirror intracellular cGMP concentrations. In this framework, VPA is predicted to reduce intracellular cGMP by inhibiting its synthesis or increasing its degradation (Fig. 6, top) and its removal increases intracellular cGMP (Fig. 6, bottom). We propose that the VPA-induced decrease in intracellular Ca^{2+} prompts a Ca^{2+}-sensitive guanylate cyclase activating protein (GCAP) to activate rGCs, as found in vertebrate photoreceptors [reviewed by [100]] and in *C. elegans* thermoreceptor neurons [125]. Such a calcium-dependent feedback mechanism is a good candidate to account for an OFF response mediated by the hypothesized increase in intracellular cGMP and TAX-4-dependent ion channel activity.

This proposed VPA signaling pathway is analogous to the canonical pathway underpinning light-dependent modulation of vertebrate photoreceptors and many of the proteins involved are conserved in *C. elegans* and in mammals, including humans. For instance, the *C. elegans* TAX-4 ion channel is orthologous to the human CNGA1 channel (51% identical) and the ODR-1 protein is orthologous to two human guanylate cyclases, GUCY2D (32% identical) and GUCY2F (34% identical). It remains to be determined whether the contribution of *odr-1* and *gcy-28* to VPA sensing is closer to the role played by rGCs in vertebrate phototransduction [100] or is instructive and modulated downstream of the Gα proteins required for VPA attraction (Fig. 6, top). In either scenario, our finding that genes encoding Gα proteins, RGS, and GRK proteins are essential for VPA attraction add evidence in favor of a role for a GPCR in VPA sensing. Although a VPA-sensitive GPCR has yet to be identified in any organism, members of this protein family are among the most pursued molecular targets for drug development and are often considered for repurposing due to their high druggability [126,127]. Identifying candidate GPCRs that might bind VPA is complicated by the widespread finding that millimolar VPA (or that of its sodium salt analog, sodium valproate), is needed to modulate the activity of neurons in mammals [70,78–85,87–90] and other animals [23–28,86]. Our work helps to establish *C. elegans* as a model organism to study the mode of action of VPA in neurons. Whereas traditional approaches have so far failed to identify the

low-affinity ligand-receptor interactions underpinning VPA's modulation of brain activity, we have shown that a non-traditional approach grounded in the sensitivity of *C. elegans* chemotaxis and chemosensory transduction combined with genetic dissection is poised to overcome this barrier.

Figure legends

Figure 1: *C. elegans* are attracted to pure VPA in a *tax-4*-dependent manner.

(A) Schematic of the 4-well chemotaxis assay plate. The locations (mm) for the start zone, VPA placement, and control (water) placement are 0, 32.5, and -32.5, respectively. Created in BioRender. Rogel-Hernandez, L. (2024). BioRender.com/y34o134. **(B)** Top: Swarm plot of the locations of individual animals (*n*, small dots) pooled across multiple assays (*N*, black dots). The mean location (gap) and standard deviation (represented by vertical lines) are shown to the right. Bottom: The bootstrapped mean difference relative to solvent controls (<Δlocation>) with its 95% confidence interval (CI). **(C)** Dose-response of VPA attraction, plotted as <Δlocation> ± 95% CI values from panel B *vs.* source concentration. The smooth line is a fit to data using a Hill equation, EC_{50} = 0.39 M, n_h = 1. **(D)** Defects in sensory cilia impairs attraction to pure VPA. Top: Small dots show the position of individual animals (*n*) pooled across multiple biological replicates (large dots, *N*). Bottom: Bootstrapped mean difference relative to WT controls with its 95% CI. **(E)** Loss of chemosensory ion channels impairs attraction to pure VPA. Top: Small dots show the position of individual animals (*n*) pooled across multiple biological replicates (large dots, *N*). Bottom: Bootstrapped mean difference relative to WT controls with its 95% CI.

Figure 2: The *tax-4*-expressing AWC CSN pair mediates attraction to VPA.

(A) Schematic showing expression of the *tax-4* and *osm-9* chemosensory ion channels in CSN pairs. Created in BioRender. Rogel-Hernandez, L. (2024) BioRender.com/v99y955. **(B-D)** VPA attraction as a function of loss of individual neurons **(B)**, neuron-specific rescue of *tax-4* expression **(C)**, and loss of AWC asymmetry **(D).** In each panel, the top row is a swarm plot of the locations of individual animals (*n*, small dots) pooled across multiple assays (*N*, black dots). The mean location (gap) and standard deviation

(represented by vertical lines) are shown to the right. Bottom: Bootstrapped mean difference relative to WT controls with its 95% CI. For ease of visual comparison, the data for *tax-4* mutants in panel B and C are replotted from Figure 1E and the data for AWC- in Figure 2D are replotted from Figure 2B. Note, *nsy-1* mutant animals give rise to animals with two AWC^{ON} neurons while *nsy-4* to those with two AWC^{OFF} neurons.

Figure 3: VPA evokes robust *tax-4*-dependent OFF responses in AWC and variable ON responses in AWB and ASH.

The neuronal activity of all amphid CSNs from control (navy blue) and *tax-4* (golden yellow) calcium imaging lines in response to VPA (6.12×10^{-4} M, $1{:}10^{-4}$ dilution) presentation and removal averaged across multiple trials (*N*). A shaded gray box indicates the 10-second VPA delivery period. Navy blue and golden yellow shaded areas represent the standard error of the mean (SEM) for control and *tax-4*, respectively.

Figure 4: Attraction to VPA is mediated by two rGCs, *odr-1* and *gcy-28*.

(A) Schematic of the expression of candidate rGC genes for the AWC CSN pair, based on Maruyama (2016) and adult CeNGEN single-cell RNA-seq dataset [38,94,95]. Gray shading indicates the presence of rGC genes. **(B)** Comparison of five rGC mutants to WT animals in VPA attraction assays. Top: Swarm plot of the locations of individual animals (*n*, small dots) pooled across multiple assays (*N*, black dots). The mean location (gap) and standard deviation (represented by vertical lines) are shown to the right. Bottom: Bootstrapped mean difference relative to WT controls with its 95% CI. **(C)** Heatmap of <Δlocation> values depicting pairwise comparisons between *tax-4*, *odr-1*, and *gcy-28* to WT in response to five compounds: isoamyl alcohol (IAA), furfural (FUR), valeric acid (VA), 2-methyl-1-butanol (2M1B), and valproic acid (VPA). Columns represent genotype comparisons, and rows represent the different attractants tested. Shades of green are positive <Δlocation> values, while shades of brown represent negative <Δlocation> values. The deeper the shade of green or brown, the greater the magnitude of the <Δlocation> value and the greater the deviation from WT behavior. **(D)** The neuronal activity of

AWC, AWB, and ASH from *odr-1* (dark green) and *gcy-28* (burnt orange) calcium imaging lines in response to VPA (6.12×10^{-4} M, $1{:}10^{-4}$ dilution) presentation and removal averaged across multiple trials (*N*). A shaded gray box indicates the 10-second VPA delivery period. Dark green and burnt orange shaded areas represent the SEM for *odr-1* and *gcy-28*, respectively. **(E)** Quantification of the signed max $\Delta F/F_0$ value during VPA presentation for AWC, AWB, and ASH across four calcium imaging lines: control, *tax-4*, *odr-1*, and *gcy-28*. Bars represent SEM and italicized numbers above tick marks in x-axis indicate the number of trials (*N*) per each CSN pair. Statistically significant comparisons ($p < 0.05$) as a function of genotype in each neuron are annotated with an asterisk (Mann-Whitney U test).

Figure 5: VPA sensing requires G proteins and GPCR signaling partners.

(A) Schematic depicting the mechanisms by which G protein subunits, RGS, β-arrestin, and GRK proteins interact with GPCRs. In its inactive state, a GPCR is bound by a heterotrimeric G protein complex. Upon ligand binding, the GPCR acts as a GEF, exchanging GDP-bound Gα for GTP, thereby dissociating the heterotrimeric G protein into two active subcomplexes (Gα and Gβγ), which recruit downstream effectors to amplify GPCR signals. RGS proteins facilitate the reversion of the Gα to the GDP-bound state. To desensitize the GPCR, GRK proteins phosphorylate the C-terminal tail of the receptor, recruiting β-arrestin and promoting its binding to the receptor. This series of events prevents the receptor from activating G proteins and its targeted for endocytosis. Created in BioRender. Rogel-Hernandez, L. (2025) https://BioRender.com/dqe4xco. **(B)** Schematic of 11 candidate Gα subunits expressed in the AWC CSN pair, based on Bastiani and Mendel (2006) and adult CeNGEN single-cell RNA-seq dataset [94,95,101]. Light blue shading indicates the presence of the Gα gene. **(C-E)** Top: Swarm plot of the locations of individual animals (*n*, small dots) pooled across multiple assays (*N*, black dots). The mean location (gap) and standard deviation (represented by vertical lines) are shown to the right. Bottom: Bootstrapped mean difference relative to WT controls with its 95% CI. Panel **(C)** compares the responses of Gα mutants to those of WT. Panel **(D)** compares the responses of *rgs-2* and *rgs-3*

mutants to those of WT. Panel **(E)** compares the responses of *arr-1*, *grk-1*, and *grk-2* mutants to those of WT.

Figure 6: Molecular model for VPA sensing in AWC.

Low cGMP state - VPA binds to and activates GPCR(s) present in the AWC neurons. This interaction results in the activation of its associated G protein, which leads to a decrease in cGMP levels inside the cell via its degradation by phosphodiesterases (PDEs) or the inhibition of its production. Consequently, lower cGMP levels result in the closing of *tax-4* ion channels, a reduction in Ca^{2+} ion influx, and hyperpolarization of the AWC neurons. **High cGMP state** - When VPA is removed or dissociates from its corresponding GPCR target(s), cGMP levels rise, *tax-4* ion channels open, cytoplasmic calcium levels increase, and the AWC neurons depolarize. Created in BioRender. Rogel-Hernandez, L. (2025) https://BioRender.com/15goo9i.

Supplementary Figure 1: Neural activity raster plots for all amphid CSN pairs in wild-type and *tax-4* mutant backgrounds.

Neural activity ($\Delta F/F_0$) raster plots for all amphid CSN pairs (in alphabetical order) across control (A) and *tax-4* (B) calcium imaging lines. Within each raster plot, rows represent individual animals sorted by mean $\Delta F/F_0$ response during VPA presentation (5-15 seconds, region encapsulated by white dashed lines). The number of animals (*N*) contributing data for each CSN pair is displayed in the lower right corner. A shared colorbar legend can be found to the right that indicates the range of $\Delta F/F_0$.

Supplementary Figure 2: The chemosensory neurons ASER, AWCL, and AWCR respond to VPA in a *tax-4*-dependent manner.

(A) The neuronal activity of ASEL, ASER, AWCL, and AWCR neurons from control (navy blue) and *tax-4* (golden yellow) calcium imaging lines in response to VPA (6.12×10^{-4} M, $1{:}10^{-4}$ dilution) presentation and removal averaged across multiple trials (*N*). A shaded gray box indicates the 10-second

VPA delivery period. Navy blue and golden yellow shaded areas represent the SEM for control and *tax-4*, respectively. **(B)** Neural activity ($\Delta F/F_0$) raster plots for ASEL, ASER, AWCL, and AWCR across control (Top) and *tax-4* (Bottom) calcium imaging lines. Within each raster plot, rows represent individual animals sorted by mean $\Delta F/F_0$ response during VPA presentation (5-15 seconds, region encapsulated by white dashed lines). The number of animals (*N*) contributing data for each CSN pair is displayed in the lower right corner. A shared colorbar legend can be found to the right that indicates the range of $\Delta F/F_0$.

Supplementary Figure 3: The chemosensory neurons AWCL and AWCR respond to VPA in an *odr-1*- and *gcy-28*-dependent manner, whereas neither ASEL nor ASER do so.

(A) Neural activity ($\Delta F/F_0$) raster plots for ASEL, ASER, AWCL, and AWCR across *odr-1* (Top) and *gcy-28* (Bottom) calcium imaging lines. Within each raster plot, rows represent individual animals sorted by mean $\Delta F/F_0$ response during VPA presentation (5-15 seconds, region encapsulated by white dashed lines). The number of animals (*N*) contributing data for each CSN pair is displayed in the lower right corner. A shared colorbar legend can be found to the right that indicates the range of $\Delta F/F_0$. **(B)** Quantification of the signed max $\Delta F/F_0$ value during VPA presentation for ASEL, ASER, AWCL, and AWCR across four calcium imaging lines: control, *tax-4*, *odr-1*, and *gcy-28*. Bars represent SEM and italicized numbers above tick marks in the x-axis indicate the number of trials (*N*) for each CSN pair. Statistically significant comparisons ($p < 0.05$) as a function of genotype in each neuron are annotated with an asterisk (Mann-Whitney U test).

Supplementary Figure 4: Neural activity raster plots for all amphid CSN pairs in *odr-1* and *gcy-28* mutant backgrounds.

Neural activity ($\Delta F/F_0$) raster plots for all amphid CSN pairs (in alphabetical order) across *odr-1* **(A)** and *gcy-28* **(B)** calcium imaging lines. Within each raster plot, rows represent individual animals sorted by mean $\Delta F/F_0$ response during VPA presentation (5-15 seconds, region encapsulated by white dashed lines).

The number of animals (*N*) contributing data for each CSN pair is displayed in the lower right corner. A shared colorbar legend can be found to the right that indicates the range of $\Delta F/F_0$.

Supplementary Figure 5: Neuronal activity of eight CSN pairs in *odr-1* and *gcy-28* mutant backgrounds that display small or no responses to VPA in wild-type.

(A) The neuronal activity of eight CSNs (ADF, ADL, ASE, ASG, ASI, ASJ, ASK, and AWA) from *odr-1* (dark green) and *gcy-28* (burnt orange) calcium imaging lines in response to VPA (6.12×10^{-4} M, $1{:}10^{-4}$ dilution) presentation and removal averaged across multiple trials (*N*). A shaded gray box indicates the 10-second VPA delivery period. Dark green and burnt orange shaded areas represent the SEM for *odr-1* and *gcy-28*, respectively. **(B)** Quantification of the signed max $\Delta F/F_0$ value during VPA presentation for ADF, ADL, ASE, ASG, ASI, ASJ, ASK, and AWA across four calcium imaging lines: control, *tax-4*, *odr-1*, and *gcy-28*. Bars represent SEM and italicized numbers above tick marks in the x-axis indicate the number of trials (*N*) for each CSN pair. Statistically significant comparisons ($p < 0.05$) as a function of genotype in each neuron are annotated with an asterisk (Mann-Whitney U test).

Acknowledgments

We thank E. Fryer, C. Jaisinghani, and Z. Liao for assistance with coding, genetics, and laboratory management, respectively, and H. Lu for conducting pilot calcium imaging studies. Other members of the Goodman laboratory helped to improve data visualization and analysis and provided valuable feedback on writing. The following investigators and their laboratories contributed *C. elegans* strains: Chen (Umeå University), Y. Iino (The University of Tokyo), and P. Sengupta (Brandeis University), and several strains were provided by the CGC, which is funded by NIH Office of Research Infrastructure Programs (P40 OD010440). This work also benefited from Wormbase [108] in its design and execution. Work supported by grants from NIH to MBG (R35NS105092) and ADTS (U01NS132158), and a Stanford BioX Bowes Interdisciplinary Graduate Fellowship and NIH training grant (T32GM113854) to LERH.

References

1. Tomson T, Battino D, Perucca E. The remarkable story of valproic acid. Lancet Neurol. 2016;15: 141.

2. Löscher W. Effects of the antiepileptic drug valproate on metabolism and function of inhibitory and excitatory amino acids in the brain. Neurochem Res. 1993;18: 485–502.

3. Keane PE, Simiand J, Mendes E, Santucci V, Morre M. The effects of analogues of valproic acid on seizures induced by pentylenetetrazol and GABA content in brain of mice. Neuropharmacology. 1983;22: 875–879.

4. Chapman AG, Meldrum BS, Mendes E. Acute anticonvulsant activity of structural analogues of valproic acid and changes in brain GABA and aspartate content. Life Sci. 1983;32: 2023–2031.

5. Snodgrass SR. GABA and epilepsy: their complex relationship and the evolution of our understanding. J Child Neurol. 1992;7: 77–86.

6. Perucca E, Bialer M, White HS. New GABA-Targeting Therapies for the Treatment of Seizures and Epilepsy: I. Role of GABA as a Modulator of Seizure Activity and Recently Approved Medications Acting on the GABA System. CNS Drugs. 2023;37: 755–779.

7. Williams RSB, Cheng L, Mudge AW, Harwood AJ. A common mechanism of action for three mood-stabilizing drugs. Nature. 2002;417: 292–295.

8. Jones GH, Rong C, Shariq AS, Mishra A, Machado-Vieira R. Intracellular Signaling Cascades in Bipolar Disorder. Curr Top Behav Neurosci. 2021;48: 101–132.

9. Terbach N, Williams RSB. Structure-function studies for the panacea, valproic acid. Biochem Soc Trans. 2009;37: 1126–1132.

10. Wu K-C, Liao K-S, Yeh L-R, Wang Y-K. Drug Repurposing: The Mechanisms and Signaling Pathways of Anti-Cancer Effects of Anesthetics. Biomedicines. 2022;10. doi:10.3390/biomedicines10071589

11. David H Coy LS. Anti-convulsant drug valproic acid in cancers and in combination anti-cancer therapeutics. Mod Chem Appl. 2014;02. doi:10.4172/2329-6798.1000118

12. Zhang CQ, He BM, Hu ML, Sun HB. Risk of Valproic Acid-Related Tremor: A Systematic Review and Meta-Analysis. Front Neurol. 2020;11: 576579.

13. Ness-Abramof R, Apovian CM. Drug-induced weight gain. Drugs Today . 2005;41: 547–555.

14. Chateauvieux S, Morceau F, Dicato M, Diederich M. Molecular and therapeutic potential and toxicity of valproic acid. J Biomed Biotechnol. 2010;2010. doi:10.1155/2010/479364

15. Perucca E. Pharmacological and therapeutic properties of valproate: A summary after 35 years of clinical experience. CNS Drugs. 2002;16: 695–714.

16. Roullet FI, Lai JKY, Foster JA. In utero exposure to valproic acid and autism--a current review of clinical and animal studies. Neurotoxicol Teratol. 2013;36: 47–56.

17. Wartman C, VandenBerg A. Valproate: Not All Boxed Warnings Are Created Equal. Ann Pharmacother. 2022;56: 1349–1355.

18. Koren G, Nava-Ocampo AA, Moretti ME, Sussman R, Nulman I. Major malformations with valproic acid. Can Fam Physician. 2006;52: 441–2, 444, 447.

19. Christensen J, Grønborg TK, Sørensen MJ, Schendel D, Parner ET, Pedersen LH, et al. Prenatal valproate exposure and risk of autism spectrum disorders and childhood autism. JAMA. 2013;309: 1696–1703.

20. Jentink J, Loane MA, Dolk H, Barisic I, Garne E, Morris JK, et al. Valproic acid monotherapy in pregnancy and major congenital malformations. N Engl J Med. 2010;362: 2185–2193.

21. Ornoy A, Echefu B, Becker M. Valproic Acid in Pregnancy Revisited: Neurobehavioral, Biochemical and Molecular Changes Affecting the Embryo and Fetus in Humans and in Animals: A Narrative Review. Int J Mol Sci. 2023;25. doi:10.3390/ijms25010390

22. Wise J. Valproate: Men planning a family should seek advice in light of neurodevelopmental disorders risk in children, says regulator. BMJ. 2024;384: q122.

23. Slater GE, Johnston D. Sodium valproate increases potassium conductance in Aplysia neurons. Epilepsia. 1978;19: 379–384.

24. Nosek TM. Depression of axonal excitability by valproate is antagonized by phenytoin. Epilepsia. 1981;22: 641–650.

25. Fohlmeister JF, Adelman WJ Jr, Brennan JJ. Excitable channel currents and gating times in the presence of anticonvulsants ethosuximide and valproate. J Pharmacol Exp Ther. 1984;230: 75–81.

26. Nosek TM. The effects of valproate and phenytoin on the cAMP and cGMP levels in nervous tissue. Proc Soc Exp Biol Med. 1985;178: 196–199.

27. VanDongen AM, VanErp MG, Voskuyl RA. Valproate reduces excitability by blockage of sodium and potassium conductance. Epilepsia. 1986;27: 177–182.

28. Kuebler D, Tanouye M. Anticonvulsant valproate reduces seizure-susceptibility in mutant Drosophila. Brain Res. 2002;958: 36–42.

29. Tokuoka SM, Saiardi A, Nurrish SJ. The mood stabilizer valproate inhibits both inositol- and diacylglycerol-signaling pathways in Caenorhabditis elegans. Mol Biol Cell. 2008;19: 2241–2250.

30. Lucanic M, Plummer WT, Chen E, Harke J, Foulger AC, Onken B, et al. Impact of genetic background and experimental reproducibility on identifying chemical compounds with robust longevity effects. Nat Commun. 2017;8: 14256.

31. Evason K, Collins JJ, Huang C, Hughes S, Kornfeld K. Valproic acid extends Caenorhabditis elegans lifespan. Aging Cell. 2008;7: 305–317.

32. Forthun RB, Sengupta T, Skjeldam HK, Lindvall JM, McCormack E, Gjertsen BT, et al. Cross-species functional genomic analysis identifies resistance genes of the histone deacetylase

inhibitor valproic acid. PLoS One. 2012;7: e48992.

33. Fryer E, Guha S, Rogel-Hernandez LE, Logan-Garbisch T, Farah H, Rezaei E, et al. A high-throughput behavioral screening platform for measuring chemotaxis by C. elegans. PLoS Biol. 2024;22: e3002672.

34. Ferkey DM, Sengupta P, L'Etoile ND. Chemosensory signal transduction in Caenorhabditis elegans. Genetics. 2021;217. doi:10.1093/genetics/iyab004

35. Wang W, Qiao Y, Li Z. New Insights into Modes of GPCR Activation. Trends Pharmacol Sci. 2018;39: 367–386.

36. Sutkeviciute I, Vilardaga J-P. Structural insights into emergent signaling modes of G protein-coupled receptors. J Biol Chem. 2020;295: 11626–11642.

37. Spehr M, Munger SD. Olfactory receptors: G protein-coupled receptors and beyond. J Neurochem. 2009;109: 1570–1583.

38. Maruyama IN. Receptor guanylyl cyclases in sensory processing. Front Endocrinol (Lausanne). 2016;7: 173.

39. Pu L, Wang J, Lu Q, Nilsson L, Philbrook A, Pandey A, et al. Dissecting the genetic landscape of GPCR signaling through phenotypic profiling in C. elegans. Nat Commun. 2023;14: 8410.

40. Quignon P, Kirkness E, Cadieu E, Touleimat N, Guyon R, Renier C, et al. Comparison of the canine and human olfactory receptor gene repertoires. Genome Biol. 2003;4: R80.

41. Policarpo M, Baldwin MW, Casane D, Salzburger W. Diversity and evolution of the vertebrate chemoreceptor gene repertoire. Nat Commun. 2024;15: 1421.

42. Ma F, Lau CY, Zheng C. Large genetic diversity and strong positive selection in F-box and GPCR genes among the wild isolates of Caenorhabditis elegans. Genome Biol Evol. 2021;13. doi:10.1093/gbe/evab048

43. Beets I, Zels S, Vandewyer E, Demeulemeester J, Caers J, Baytemur E, et al. System-wide mapping of peptide-GPCR interactions in C. elegans. Cell Rep. 2023;42: 113058.

44. Thomas JH, Robertson HM. The Caenorhabditis chemoreceptor gene families. BMC Biol. 2008;6: 42.

45. Stiernagle T. Maintenance of C. elegans. WormBook. 2006; 1–11.

46. Bulterijs S, Braeckman BP. Phenotypic Screening in C. elegans as a Tool for the Discovery of New Geroprotective Drugs. Pharmaceuticals . 2020;13. doi:10.3390/ph13080164

47. Lin A, Qin S, Casademunt H, Wu M, Hung W, Cain G, et al. Functional imaging and quantification of multineuronal olfactory responses in *C. elegans*. Sci Adv. 2023;9: eade1249.

48. Fryer E, Guha S, Rogel-Hernandez LE, Logan-Garbisch T, Farah H, Rezaei E, et al. A high-throughput behavioral screening platform for measuring chemotaxis by C. elegans. PLoS Biol. 2024;22: e3002672.

49. Stroustrup N, Ulmschneider BE, Nash ZM, López-Moyado IF, Apfeld J, Fontana W. The

Caenorhabditis elegans Lifespan Machine. Nat Methods. 2013;10: 665–670.

50. Ho J, Tumkaya T, Aryal S, Choi H, Claridge-Chang A. Moving beyond P values: data analysis with estimation graphics. Nat Methods. 2019;16: 565–566.

51. Prinz H. Hill coefficients, dose-response curves and allosteric mechanisms. J Chem Biol. 2010;3: 37–44.

52. Virtanen P, Gommers R, Oliphant TE, Haberland M, Reddy T, Cournapeau D, et al. SciPy 1.0: fundamental algorithms for scientific computing in Python. Nat Methods. 2020;17: 261–272.

53. White JG, Southgate E, Thomson JN, Brenner S. The structure of the nervous system of the nematode Caenorhabditis elegans. Philos Trans R Soc Lond B Biol Sci. 1986;314: 1–340.

54. Mann HB, Whitney DR. On a Test of Whether one of Two Random Variables is Stochastically Larger than the Other. Ann Math Statist. 1947;18: 50–60.

55. Heiman MG, Shaham S. DEX-1 and DYF-7 establish sensory dendrite length by anchoring dendritic tips during cell migration. Cell. 2009;137: 344–355.

56. Heiman MG, Shaham S. DEX-1 and DYF-7 establish sensory dendrite length by anchoring dendritic tips during cell migration. Cell. 2009;137: 344–355.

57. Starich TA, Herman RK, Kari CK, Yeh WH, Schackwitz WS, Schuyler MW, et al. Mutations affecting the chemosensory neurons of Caenorhabditis elegans. Genetics. 1995;139: 171–188.

58. Howell K, Hobert O. Morphological Diversity of C. elegans Sensory Cilia Instructed by the Differential Expression of an Immunoglobulin Domain Protein. Curr Biol. 2017;27: 1782–1790.e5.

59. Logan-Garbisch T, Fryer E, Seyahi LS, Rogel-Hernandez L, Rhee SY, Goodman MB. Satiety, TAX-4, and OSM-9 Tune the Attraction of C. elegans Nematodes to Microbial Fermentation Products. Neuroscience. bioRxiv; 2025. Available: https://www.biorxiv.org/content/10.1101/2025.02.21.639594v1

60. Chelur DS, Chalfie M. Targeted cell killing by reconstituted caspases. Proc Natl Acad Sci U S A. 2007;104: 2283–2288.

61. Komatsu H, Mori I, Rhee JS, Akaike N, Ohshima Y. Mutations in a cyclic nucleotide-gated channel lead to abnormal thermosensation and chemosensation in C. elegans. Neuron. 1996;17: 707–718.

62. Coates JC, de Bono M. Antagonistic pathways in neurons exposed to body fluid regulate social feeding in Caenorhabditis elegans. Nature. 2002;419: 925–929.

63. Uchida O, Nakano H, Koga M, Ohshima Y. The C. elegans che-1 gene encodes a zinc finger transcription factor required for specification of the ASE chemosensory neurons. Development. 2003;130: 1215–1224.

64. Yoshida K, Hirotsu T, Tagawa T, Oda S, Wakabayashi T, Iino Y, et al. Odour concentration-dependent olfactory preference change in C. elegans. Nat Commun. 2012;3: 739.

65. Sagasti A, Hobert O, Troemel E, Ruvkun G, Bargmann C. Alternative olfactory neuron fates are specified by the LIM homeobox gene lim-4. Genes Dev. 1999;13: 1794–1806.

66. Colosimo ME, Tran S, Sengupta P. The divergent orphan nuclear receptor ODR-7 regulates olfactory neuron gene expression via multiple mechanisms in Caenorhabditis elegans. Genetics. 2003;165: 1779–1791.

67. Hsieh Y-W, Alqadah A, Chuang C-F. Asymmetric neural development in the Caenorhabditis elegans olfactory system. Genesis. 2014;52: 544–554.

68. Lesch BJ, Gehrke AR, Bulyk ML, Bargmann CI. Transcriptional regulation and stabilization of left-right neuronal identity in C. elegans. Genes Dev. 2009;23: 345–358.

69. Čapek R, Esplin B. Mechanisms of anticonvulsant action of valproate: An overview and perspective. Generalized Epilepsy. Boston, MA: Birkhäuser Boston; 1990. pp. 436–459.

70. Van den Berg RJ, Kok P, Voskuyl RA. Valproate and sodium currents in cultured hippocampal neurons. Exp Brain Res. 1993;93: 279–287.

71. Rahman M, Awosika AO, Nguyen H. Valproic acid. StatPearls. Treasure Island (FL): StatPearls Publishing; 2025.

72. Schierscher T, Salzmann L, Singh N, Fleischer S, Schäfer C, Hoop J, et al. An isotope dilution-liquid-chromatography-tandem mass spectrometry-based candidate reference measurement procedure for the quantification of total and free valproic acid in human serum and plasma. Clin Chem Lab Med. 2025. doi:10.1515/cclm-2025-1053

73. Chalasani SH, Chronis N, Tsunozaki M, Gray JM, Ramot D, Goodman MB, et al. Dissecting a circuit for olfactory behaviour in Caenorhabditis elegans. Nature. 2016;450: 63–70.

74. Akerboom J, Chen T-W, Wardill TJ, Tian L, Marvin JS, Mutlu S, et al. Optimization of a GCaMP calcium indicator for neural activity imaging. J Neurosci. 2012;32: 13819–13840.

75. Hsueh Y-P, Gronquist MR, Schwarz EM, Nath RD, Lee C-H, Gharib S, et al. Nematophagous fungus Arthrobotrys oligospora mimics olfactory cues of sex and food to lure its nematode prey. Elife. 2017;6. doi:10.7554/eLife.20023

76. Brissette B, Ficaro L, Li C, Jones DR, Ramanathan S, Ringstad N. Chemosensory detection of polyamine metabolites guides C. elegans to nutritive microbes. Sci Adv. 2024;10: eadj4387.

77. Pandey A, Katz M, Nurrish S, Philbrook A, Sengupta P. A lateralized sensory signaling pathway mediates context-dependent olfactory plasticity in C. elegans. bioRxivorg. 2025. doi:10.1101/2025.07.25.666858

78. Harrison NL, Simmonds MA. Sodium valproate enhances responses to GABA receptor activation only at high concentrations. Brain Res. 1982;250: 201–204.

79. Olpe HR, Steinmann MW, Pozza MF, Brugger F, Schmutz M. Valproate enhances GABA-A mediated inhibition of locus coeruleus neurones in vitro. Naunyn Schmiedebergs Arch Pharmacol. 1988;338: 655–657.

80. Zona C, Avoli M. Effects induced by the antiepileptic drug valproic acid upon the ionic currents recorded in rat neocortical neurons in cell culture. Exp Brain Res. 1990;81: 313–317.

81. Zeise ML, Kasparow S, Zieglgänsberger W. Valproate suppresses N-methyl-D-aspartate-evoked, transient depolarizations in the rat neocortex in vitro. Brain Res. 1991;544: 345–348.

82. Gean PW, Huang CC, Hung CR, Tsai JJ. Valproic acid suppresses the synaptic response mediated by the NMDA receptors in rat amygdalar slices. Brain Res Bull. 1994;33: 333–336.

83. Cunningham MO, Woodhall GL, Jones RSG. Valproate modifies spontaneous excitation and inhibition at cortical synapses in vitro. Neuropharmacology. 2003;45: 907–917.

84. Martín ED, Pozo MA. Valproate reduced synaptic activity increase induced by 4-aminopyridine at the hippocampal CA3-CA1 synapse. Epilepsia. 2004;45: 436–440.

85. Yong W, Zhang M-M, Wang S, Ruan D-Y. Effects of sodium valproate on synaptic transmission and neuronal excitability in rat hippocampus. Clin Exp Pharmacol Physiol. 2009;36: 1062–1067.

86. Kautu BB, Carrasquilla A, Hicks ML, Caldwell KA, Caldwell GA. Valproic acid ameliorates C. elegans dopaminergic neurodegeneration with implications for ERK-MAPK signaling. Neurosci Lett. 2013;541: 116–119.

87. Wang S-Y, Ren M, Jiang H-Z, Wang J, Jiang H-Q, Yin X, et al. Notch pathway is activated in cell culture and mouse models of mutant SOD1-related familial amyotrophic lateral sclerosis, with suppression of its activation as an additional mechanism of neuroprotection for lithium and valproate. Neuroscience. 2015;301: 276–288.

88. Kay HY, Greene DL, Kang S, Kosenko A, Hoshi N. M-current preservation contributes to anticonvulsant effects of valproic acid. J Clin Invest. 2015;125: 3904–3914.

89. Zhang C, Yuan X, Hu Z, Liu S, Li H, Wu M, et al. Valproic Acid Protects Primary Dopamine Neurons from MPP+-Induced Neurotoxicity: Involvement of GSK3β Phosphorylation by Akt and ERK through the Mitochondrial Intrinsic Apoptotic Pathway. Biomed Res Int. 2017;2017: 8124501.

90. MacKeigan D, Feja M, Meller S, Deking L, Javadova A, Veenhuis A, et al. Long-lasting antiseizure effects of chronic intrasubthalamic convection-enhanced delivery of valproate. Neurobiol Dis. 2023;187: 106321.

91. Alqadah A, Hsieh Y-W, Xiong R, Chuang C-F. Stochastic left-right neuronal asymmetry in Caenorhabditis elegans. Philos Trans R Soc Lond B Biol Sci. 2016;371. doi:10.1098/rstb.2015.0407

92. Cochella L, Tursun B, Hsieh Y-W, Galindo S, Johnston RJ, Chuang C-F, et al. Two distinct types of neuronal asymmetries are controlled by the Caenorhabditis elegans zinc finger transcription factor die-1. Genes Dev. 2014;28: 34–43.

93. Maruyama IN. Receptor Guanylyl Cyclases in Sensory Processing. Front Endocrinol . 2016;7: 173.

94. Taylor SR, Santpere G, Weinreb A, Barrett A, Reilly MB, Xu C, et al. Molecular topography of an entire nervous system. Cell. 2021;184: 4329–4347.e23.

95. Taylor SR, McWhirter RD, Matlock BK, Flaherty DK, Miller DM 3rd. Protocol for isolating specific C. elegans neuron types for bulk and single-cell RNA sequencing. STAR Protoc. 2024;5: 103439.

96. L'Etoile ND, Bargmann CI. Olfaction and odor discrimination are mediated by the C. elegans guanylyl cyclase ODR-1. Neuron. 2000;25: 575–586.

97. Sarkar S, Rogel-Hernandez LE, Logan-Garbisch T, Fryer E, Johnson V, Goodman MB. Valeric acid attracts C. elegans by activating the AWC neurons through a tax-4 -dependent signaling pathway. MicroPubl Biol. 2025;2025. doi:10.17912/micropub.biology.001630

98. Tsunozaki M, Chalasani SH, Bargmann CI. A behavioral switch: cGMP and PKC signaling in olfactory neurons reverses odor preference in C. elegans. Neuron. 2008;59: 959–971.

99. Wacker D, Stevens RC, Roth BL. How ligands illuminate GPCR molecular pharmacology. Cell. 2017;170: 414–427.

100. Arshavsky VY, Burns ME. Photoreceptor signaling: supporting vision across a wide range of light intensities. J Biol Chem. 2012;287: 1620–1626.

101. Bastiani C, Mendel J. Heterotrimeric G proteins in C. elegans. WormBook. 2006; 1–25.

102. Palmitessa A, Hess HA, Bany IA, Kim Y-M, Koelle MR, Benovic JL. Caenorhabditus elegans Arrestin Regulates Neural G Protein Signaling and Olfactory Adaptation and Recovery*. J Biol Chem. 2005;280: 24649–24662.

103. Dong MQ, Chase D, Patikoglou GA, Koelle MR. Multiple RGS proteins alter neural G protein signaling to allow C. elegans to rapidly change behavior when fed. Genes Dev. 2000;14: 2003–2014.

104. Dixit A, Sandhu A, Modi S, Shashikanth M, Koushika SP, Watts JL, et al. Neuronal control of lipid metabolism by STR-2 G protein-coupled receptor promotes longevity in Caenorhabditis elegans. Aging Cell. 2020;19: e13160.

105. Matúš D, Prömel S. G Proteins and GPCRs in C. elegans Development: A Story of Mutual Infidelity. J Dev Biol. 2018;6. doi:10.3390/jdb6040028

106. Roayaie K, Crump JG, Sagasti A, Bargmann CI. The G alpha protein ODR-3 mediates olfactory and nociceptive function and controls cilium morphogenesis in C. elegans olfactory neurons. Neuron. 1998;20: 55–67.

107. Campagna CM, McMahon H, Nechipurenko I. The G protein alpha chaperone and guanine-nucleotide exchange factor RIC-8 regulates cilia morphogenesis in Caenorhabditis elegans sensory neurons. PLoS Genet. 2023;19: e1011015.

108. Sternberg PW, Van Auken K, Wang Q, Wright A, Yook K, Zarowiecki M, et al. WormBase 2024: status and transitioning to Alliance infrastructure. Genetics. 2024;227. doi:10.1093/genetics/iyae050

109. Ferkey DM, Hyde R, Haspel G, Dionne HM, Hess HA, Suzuki H, et al. C. elegans G protein regulator RGS-3 controls sensitivity to sensory stimuli. Neuron. 2007;53: 39–52.

110. Lefkowitz RJ, Rajagopal K, Whalen EJ. New roles for beta-arrestins in cell signaling: not just for seven-transmembrane receptors. Mol Cell. 2006;24: 643–652.

111. Gurevich VV, Gurevich EV. GPCR Signaling Regulation: The Role of GRKs and Arrestins. Front Pharmacol. 2019;10: 125.

112. Chaudhary PK, Kim S. The GRKs Reactome: Role in Cell Biology and Pathology. Int J Mol Sci. 2021;22. doi:10.3390/ijms22073375

113. Fukuto HS, Ferkey DM, Apicella AJ, Lans H, Sharmeen T, Chen W, et al. G protein-coupled receptor kinase function is essential for chemosensation in C. elegans. Neuron. 2004;42: 581–593.

114. Wood JF, Ferkey DM. GRK Roles in C. elegans. In: Gurevich VV, Gurevich EV, Tesmer JJG, editors. G Protein-Coupled Receptor Kinases. New York, NY: Springer New York; 2016. pp.

283–299.

115. Philbrook A, O'Donnell MP, Grunenkovaite L, Sengupta P. Cilia structure and intraflagellar transport differentially regulate sensory response dynamics within and between C. elegans chemosensory neurons. PLoS Biol. 2024;22: e3002892.

116. Taylor SR, Santpere G, Weinreb A, Barrett A, Reilly MB, Xu C, et al. Molecular topography of an entire nervous system. Cell. 2021;184: 4329–4347.e23.

117. Krzyzanowski MC, Woldemariam S, Wood JF, Chaubey AH, Brueggemann C, Bowitch A, et al. Aversive behavior in the nematode C. elegans is modulated by cGMP and a neuronal gap junction network. PLoS Genet. 2016;12: e1006153.

118. Potter LR. Guanylyl cyclase structure, function and regulation. Cell Signal. 2011;23: 1921–1926.

119. Murayama T, Takayama J, Fujiwara M, Maruyama IN. Environmental alkalinity sensing mediated by the transmembrane guanylyl cyclase GCY-14 in C. elegans. Curr Biol. 2013;23: 1007–1012.

120. Smith ESJ, Martinez-Velazquez L, Ringstad N. A chemoreceptor that detects molecular carbon dioxide. J Biol Chem. 2013;288: 37071–37081.

121. Zhu M, Chen Y, Zhao N, Bai H, Zhang K, Huang X. Multiple olfactory pathways contribute to the lure process of Caenorhabditis elegans by pathogenic bacteria. Sci China Life Sci. 2021;64: 1346–1354.

122. Zhang C, Zhao N, Chen Y, Zhang D, Yan J, Zou W, et al. The signaling pathway of Caenorhabditis elegans mediates chemotaxis response to the attractant 2-heptanone in a Trojan Horse-like pathogenesis. J Biol Chem. 2016;291: 23618–23627.

123. Chalasani SH, Chronis N, Tsunozaki M, Gray JM, Ramot D, Goodman MB, et al. Dissecting a circuit for olfactory behaviour in Caenorhabditis elegans. Nature. 2007;450: 63–70.

124. Cheng H, Liu Y, Xue Y, Shao J, Tan Z, Liu S, et al. Molecular Strategies for Intensity-Dependent Olfactory Processing in Caenorhabditis elegans. Front Mol Neurosci. 2021;14: 748214.

125. Wang D, O'Halloran D, Goodman MB. GCY-8, PDE-2, and NCS-1 are critical elements of the cGMP-dependent thermotransduction cascade in the AFD neurons responsible for C. elegans thermotaxis. J Gen Physiol. 2013;142: 437–449.

126. de Felice A, Aureli S, Limongelli V. Drug repurposing on G protein-coupled receptors using a Computational Profiling approach. Front Mol Biosci. 2021;8: 673053.

127. Lorente JS, Sokolov AV, Ferguson G, Schiöth HB, Hauser AS, Gloriam DE. GPCR drug discovery: new agents, targets and indications. Nat Rev Drug Discov. 2025;24: 458–479.

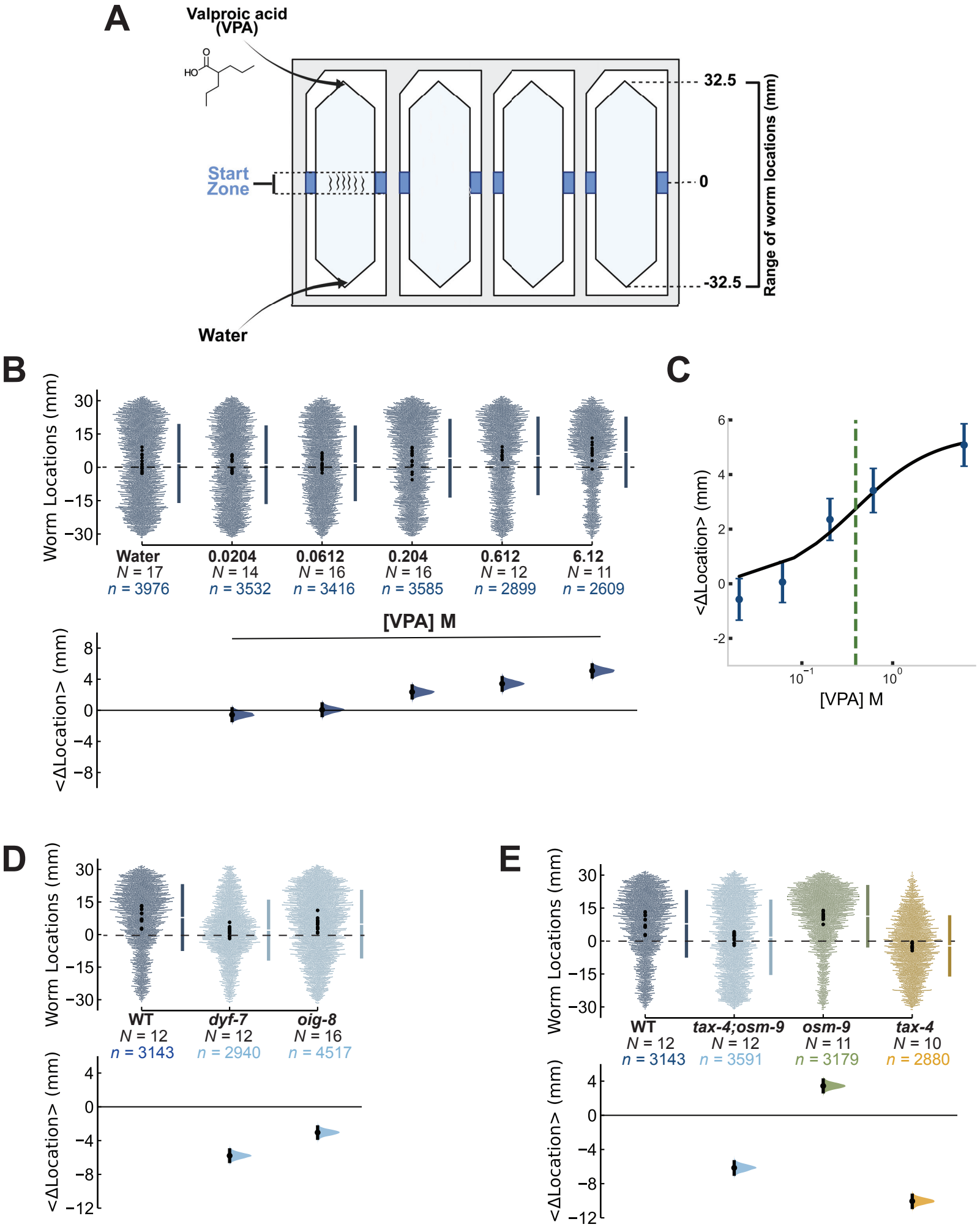
A
Valproic acid (VPA)
HO
O
Start Zone
Water
32.5
0
-32.5
Range of worm locations (mm)
B
Worm Locations (mm)
30
15
0
−15
−30
Water
N = 17
n = 3976
0.0204
N = 14
n = 3532
0.0612
N = 16
n = 3416
0.204
N = 16
n = 3585
0.612
N = 12
n = 2899
6.12
N = 11
n = 2609
[VPA] M
<ΔLocation> (mm)
8
4
0
−4
−8
C
<ΔLocation> (mm)
6
4
2
0
-2
10^−1
10^0
[VPA] M
D
Worm Locations (mm)
WT
N = 12
n = 3143
dyf-7
N = 12
n = 2940
oig-8
N = 16
n = 4517
<ΔLocation> (mm)
4
0
−4
−8
−12
E
Worm Locations (mm)
WT
N = 12
n = 3143
tax-4;osm-9
N = 12
n = 3591
osm-9
N = 11
n = 3179
tax-4
N = 10
n = 2880
<ΔLocation> (mm)

Figure 1

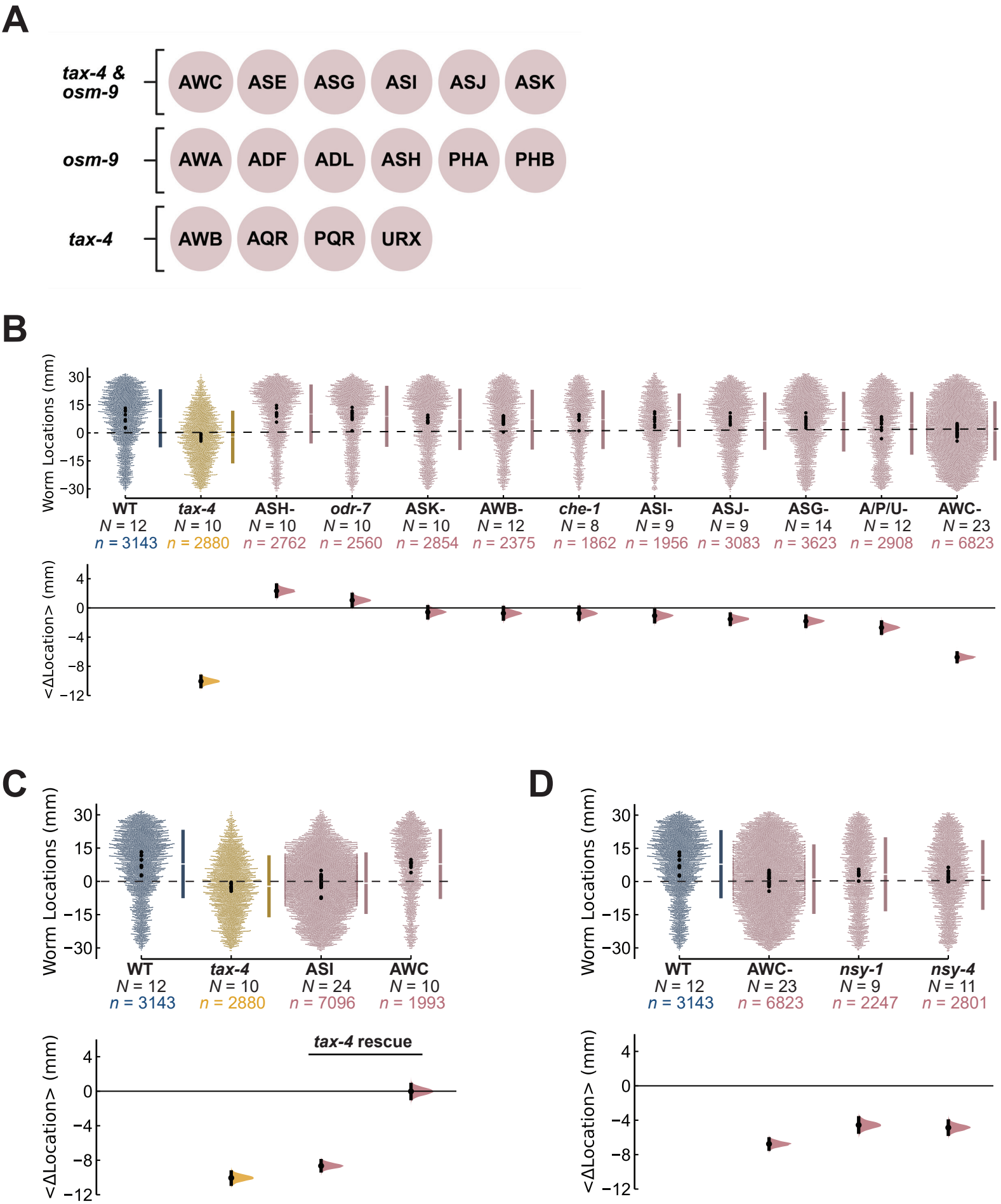
A
tax-4 & osm-9
AWC
ASE
ASG
ASI
ASJ
ASK
osm-9
AWA
ADF
ADL
ASH
PHA
PHB
tax-4
AWB
AQR
PQR
URX
B
Worm Locations (mm)
30
15
0
−15
−30
WT
N = 12
n = 3143
tax-4
N = 10
n = 2880
ASH-
N = 10
n = 2762
odr-7
N = 10
n = 2560
ASK-
N = 10
n = 2854
AWB-
N = 12
n = 2375
che-1
N = 8
n = 1862
ASI-
N = 9
n = 1956
ASJ-
N = 9
n = 3083
ASG-
N = 14
n = 3623
A/P/U-
N = 12
n = 2908
AWC-
N = 23
n = 6823
<ΔLocation> (mm)
4
0
−4
−8
−12
C
Worm Locations (mm)
30
15
0
−15
−30
WT
N = 12
n = 3143
tax-4
N = 10
n = 2880
ASI
N = 24
n = 7096
AWC
N = 10
n = 1993
tax-4 rescue
<ΔLocation> (mm)
4
0
−4
−8
−12
D
Worm Locations (mm)
30
15
0
−15
−30
WT
N = 12
n = 3143
AWC-
N = 23
n = 6823
nsy-1
N = 9
n = 2247
nsy-4
N = 11
n = 2801
<ΔLocation> (mm)
4
0
−4
−8
−12

Figure 2

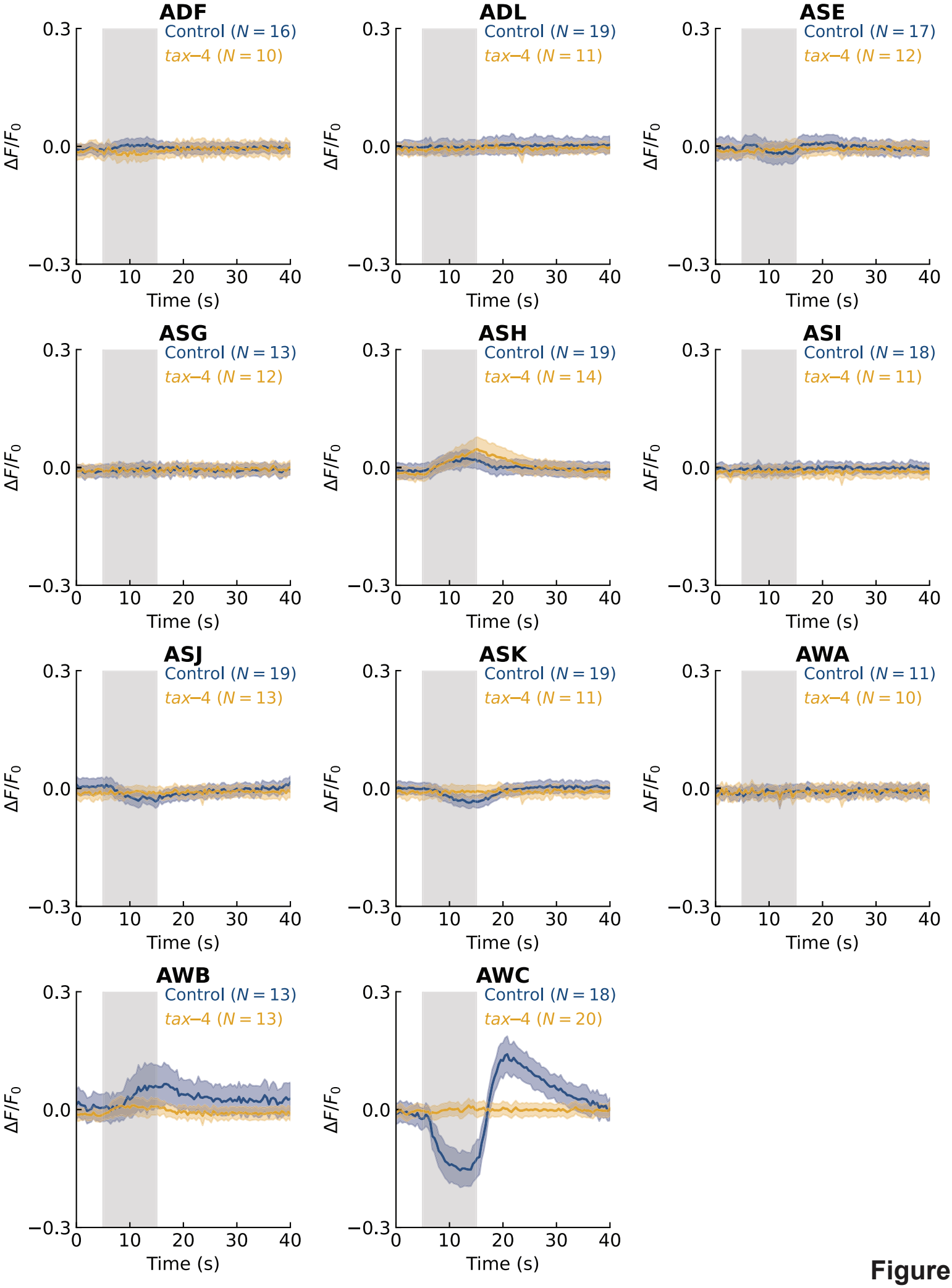
ADF
Control (N = 16)
tax–4 (N = 10)
ADL
Control (N = 19)
tax–4 (N = 11)
ASE
Control (N = 17)
tax–4 (N = 12)
ASG
Control (N = 13)
tax–4 (N = 12)
ASH
Control (N = 19)
tax–4 (N = 14)
ASI
Control (N = 18)
tax–4 (N = 11)
ASJ
Control (N = 19)
tax–4 (N = 13)
ASK
Control (N = 19)
tax–4 (N = 11)
AWA
Control (N = 11)
tax–4 (N = 10)
AWB
Control (N = 13)
tax–4 (N = 13)
AWC
Control (N = 18)
tax–4 (N = 20)
ΔF/F0
0.3
0.0
−0.3
0
10
20
30
40
Time (s)

Figure 3

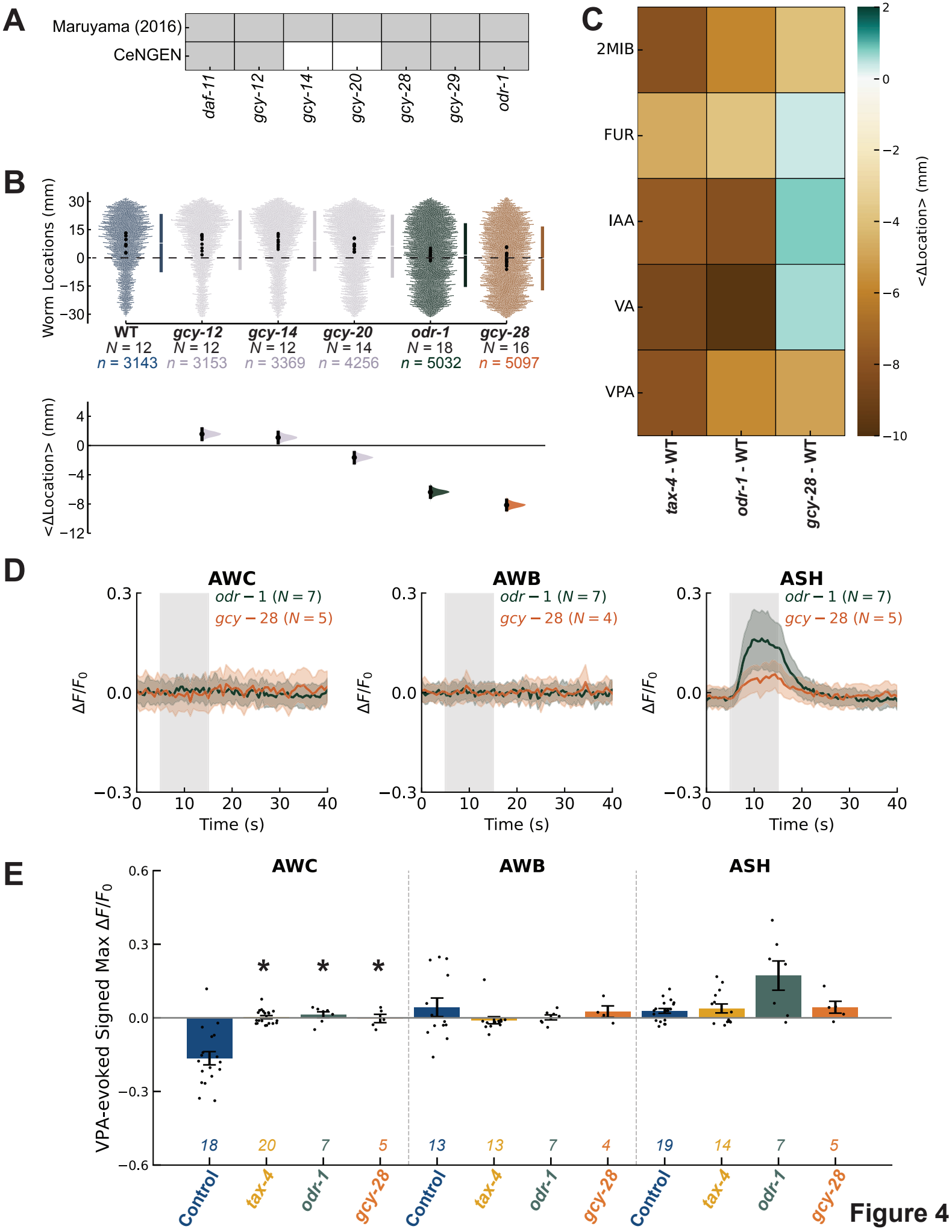
A
Maruyama (2016)
CeNGEN
daf-11
gcy-12
gcy-14
gcy-20
gcy-28
gcy-29
odr-1
B
Worm Locations (mm)
WT
N = 12
n = 3143
gcy-12
N = 12
n = 3153
gcy-14
N = 12
n = 3369
gcy-20
N = 14
n = 4256
odr-1
N = 18
n = 5032
gcy-28
N = 16
n = 5097
<ΔLocation> (mm)
C
2MIB
FUR
IAA
VA
VPA
tax-4 - WT
odr-1 - WT
gcy-28 - WT
<ΔLocation> (mm)
D
AWC
odr − 1 (N = 7)
gcy − 28 (N = 5)
AWB
odr − 1 (N = 7)
gcy − 28 (N = 4)
ASH
odr − 1 (N = 7)
gcy − 28 (N = 5)
ΔF/F0
Time (s)
E
AWC
AWB
ASH
VPA-evoked Signed Max ΔF/F0
18
20
7
5
13
13
7
4
19
14
7
5
Control
tax-4
odr-1
gcy-28
Control
tax-4
odr-1
gcy-28
Control
tax-4
odr-1
gcy-28

Figure 4

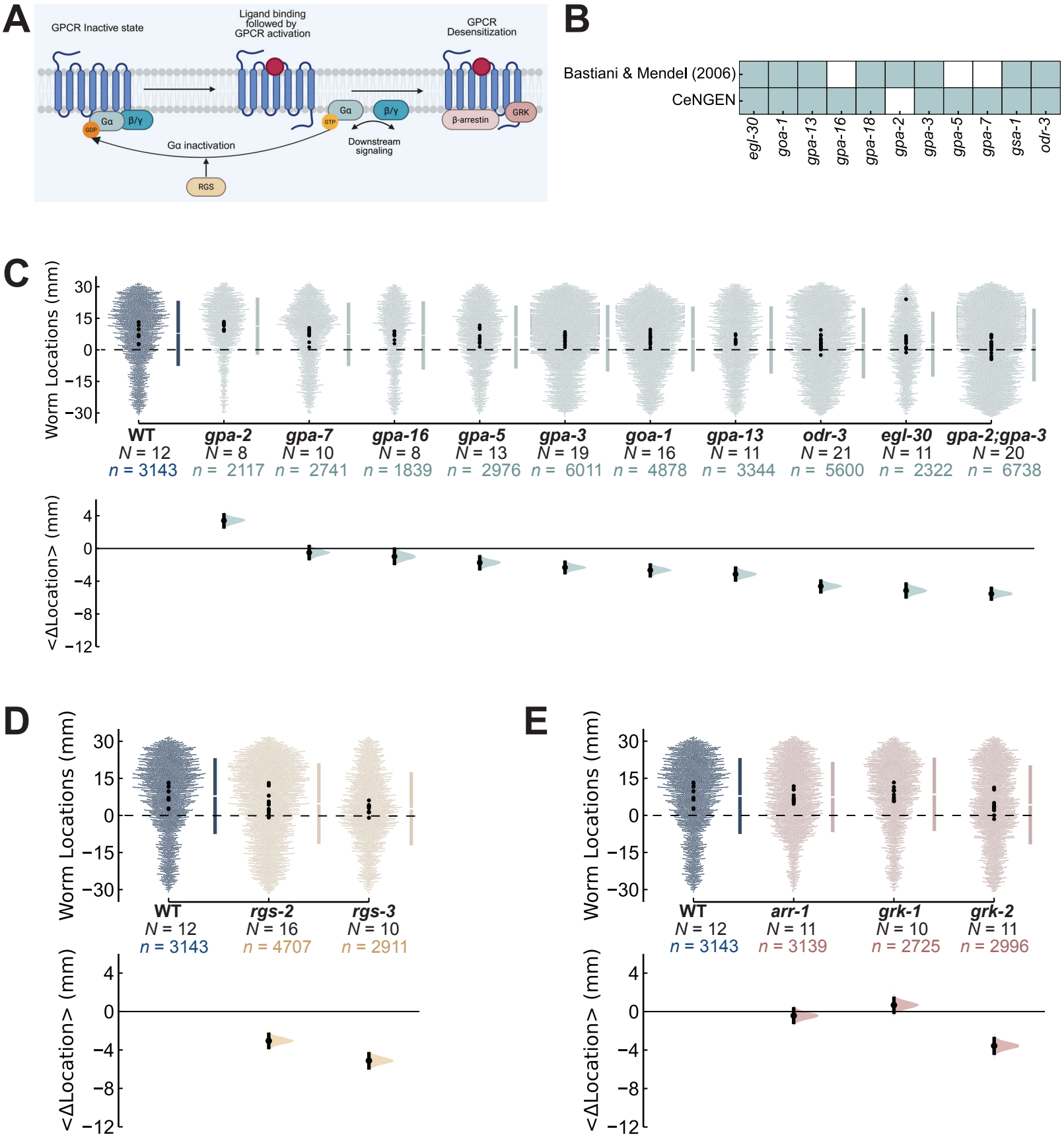
A
GPCR Inactive state
Ligand binding followed by GPCR activation
GPCR Desensitization
Gα
β/γ
GDP
GTP
β-arrestin
GRK
Gα inactivation
Downstream signaling
RGS
B
Bastiani & Mendel (2006)
CeNGEN
egl-30
goa-1
gpa-13
gpa-16
gpa-18
gpa-2
gpa-3
gpa-5
gpa-7
gsa-1
odr-3
C
Worm Locations (mm)
WT N = 12 n = 3143
gpa-2 N = 8 n = 2117
gpa-7 N = 10 n = 2741
gpa-16 N = 8 n = 1839
gpa-5 N = 13 n = 2976
gpa-3 N = 19 n = 6011
goa-1 N = 16 n = 4878
gpa-13 N = 11 n = 3344
odr-3 N = 21 n = 5600
egl-30 N = 11 n = 2322
gpa-2;gpa-3 N = 20 n = 6738
<ΔLocation> (mm)
D
Worm Locations (mm)
WT N = 12 n = 3143
rgs-2 N = 16 n = 4707
rgs-3 N = 10 n = 2911
<ΔLocation> (mm)
E
Worm Locations (mm)
WT N = 12 n = 3143
arr-1 N = 11 n = 3139
grk-1 N = 10 n = 2725
grk-2 N = 11 n = 2996
<ΔLocation> (mm)

Figure 5

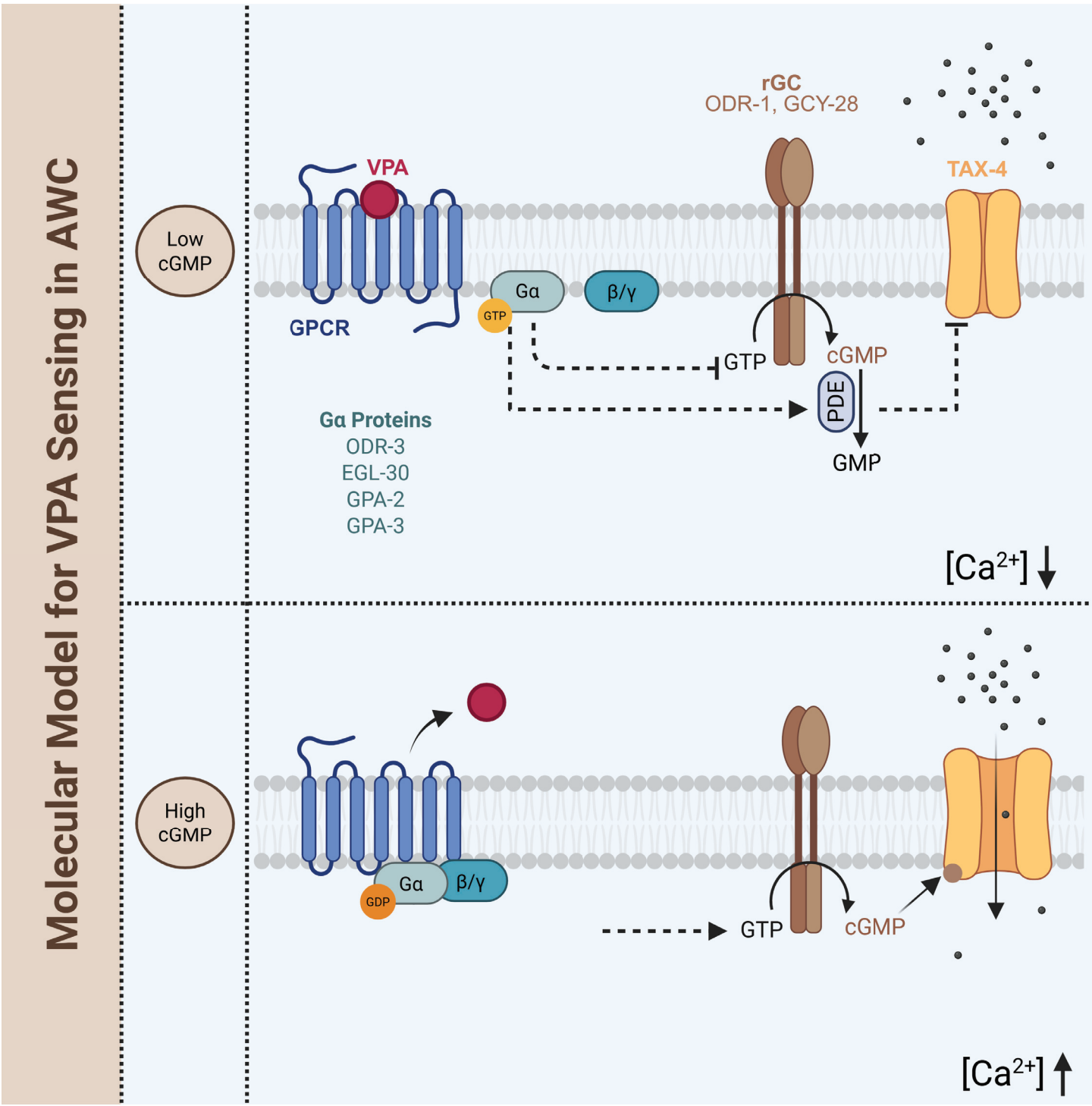
Molecular Model for VPA Sensing in AWC
Low cGMP
VPA
GPCR
Gα
GTP
β/γ
rGC
ODR-1, GCY-28
TAX-4
GTP
cGMP
PDE
GMP
Gα Proteins
ODR-3
EGL-30
GPA-2
GPA-3
[Ca2+]
High cGMP
Gα
GDP
β/γ
GTP
cGMP
[Ca2+]

Figure 6